

Chulalongkorn University

Chula Digital Collections

Chulalongkorn University Theses and Dissertations (Chula ETD)

2022

Sulfur-tolerant cobalt-doped La_{0.3}Sr_{0.7}TiO₃-d-perovskite cathode for intermediate-temperature solid oxide electrolysis cell

Natthamon Nuengjumnong
Faculty of Engineering

Follow this and additional works at: <https://digital.car.chula.ac.th/chulaetd>

 Part of the [Chemical Engineering Commons](#)

Recommended Citation

Nuengjumnong, Natthamon, "Sulfur-tolerant cobalt-doped La_{0.3}Sr_{0.7}TiO₃-d-perovskite cathode for intermediate-temperature solid oxide electrolysis cell" (2022). *Chulalongkorn University Theses and Dissertations (Chula ETD)*. 5766.
<https://digital.car.chula.ac.th/chulaetd/5766>

This Thesis is brought to you for free and open access by Chula Digital Collections. It has been accepted for inclusion in Chulalongkorn University Theses and Dissertations (Chula ETD) by an authorized administrator of Chula Digital Collections. For more information, please contact ChulaDC@car.chula.ac.th.

Sulfur-tolerant cobalt-doped $\text{La}_{0.3}\text{Sr}_{0.7}\text{TiO}_{3-\delta}$ -perovskite cathode for intermediate-temperature solid oxide electrolysis cell



Miss Natthamon Nuengjumnong

A Thesis Submitted in Partial Fulfillment of the Requirements
for the Degree of Master of Engineering in Chemical Engineering

Department of Chemical Engineering

FACULTY OF ENGINEERING

Chulalongkorn University

Academic Year 2022

Copyright of Chulalongkorn University

ข้าวแคโทดประเภทเพอรอฟสไกต์ $\text{La}_{0.3}\text{Sr}_{0.7}\text{TiO}_{3-d}$ เจือด้วยโคบอลต์ที่ทนต่อซัลเฟอร์สำหรับเซลล์อเล็ก
โทรไลซิสแบบออกไซด์ของแข็งชนิดอุณหภูมิปานกลาง



วิทยานิพนธ์นี้เป็นส่วนหนึ่งของการศึกษาตามหลักสูตรปริญญาวิศวกรรมศาสตรมหาบัณฑิต
สาขาวิชาวิศวกรรมเคมี ภาควิชาวิศวกรรมเคมี
คณะวิศวกรรมศาสตร์ จุฬาลงกรณ์มหาวิทยาลัย
ปีการศึกษา 2565
ลิขสิทธิ์ของจุฬาลงกรณ์มหาวิทยาลัย

Thesis Title	Sulfur-tolerant cobalt-doped $\text{La}_{0.3}\text{Sr}_{0.7}\text{TiO}_{3-\text{d}}$ -perovskite cathode for intermediate-temperature solid oxide electrolysis cell
By	Miss Natthamon Nuengjumnong
Field of Study	Chemical Engineering
Thesis Advisor	Associate Professor PATTARAPORN KIM, Ph.D.

Accepted by the FACULTY OF ENGINEERING, Chulalongkorn University in
Partial Fulfillment of the Requirement for the Master of Engineering

..... Dean of the FACULTY OF
ENGINEERING
(Professor SUPOT TEACHAVORASINSKUN, D.Eng.)

THESIS COMMITTEE

..... Chairman
(Professor ANONGNAT SOMWANGTHANAROJ, Ph.D.)

..... Thesis Advisor
(Associate Professor PATTARAPORN KIM, Ph.D.)

..... Examiner
(Assistant Professor SUPHOT PHATANASRI, D.Eng.)

..... External Examiner
(Associate Professor Panpailin Seeharaj, Ph.D.)

ณัฐมล เนื่องจํานงค์ : ขั้วแคโทดประเภทเพอรอฟสไกต์ $\text{La}_{0.3}\text{Sr}_{0.7}\text{TiO}_{3-d}$ เจือด้วยโคบอลต์ที่ทนต่อซัลเฟอร์สำหรับเซลล์อิเล็กโทรไลซิสแบบออกไซด์ของแข็งชนิดอุณหภูมิปานกลาง. (Sulfur-tolerant cobalt-doped $\text{La}_{0.3}\text{Sr}_{0.7}\text{TiO}_{3-d}$ -perovskite cathode for intermediate-temperature solid oxide electrolysis cell) อ.ที่ปรึกษาหลัก : ภัทรพร คิม

ขั้วแคโทด $\text{La}_{0.3}\text{Sr}_{0.7}\text{TiO}_{3.6}$ (LST) ขั้วเป็นแคโทดประเภทเพอรอฟสไกต์ในเซลล์อิเล็กโทรไลซิสแบบออกไซด์ของแข็ง (SOEC) ซึ่งมีความสามารถในการผลิตก๊าซสังเคราะห์จาก CO_2 และไอน้ำ อย่างไรก็ตามแคโทดประเภท LST ยังคงขาดความเสถียรภาพทางโครงสร้างเคมี นอกจากนี้กํามะถันอาจส่งผลต่อความทนทานซึ่งส่งผลต่อความทนทานในการใช้งาน ดังนั้นเพื่อปรับปรุงความเสถียรภาพ และความทนทานต่อกํามะถัน จึงทำการสังเคราะห์ขั้วแคโทดเพอรอฟสไกต์ $\text{La}_{0.3}\text{Sr}_{0.7}\text{Ti}_{1-y}\text{Co}_y\text{O}_{3.6}$ (LSTC) โดยการเติมไอออนโลหะ Co^{2+} ที่ตำแหน่ง B-site เมื่อ y มีค่าเท่ากับ 0 ถึง 20 เปอร์เซ็นต์โมล โดยสังเคราะห์ด้วยวิธีการเผาไหม้กรดซิตริก-ไนเตรด จากการวิเคราะห์ด้วยเทคนิคเลี้ยวเบนของรังสีเอกซ์พบว่าตัวอย่างชนิด LSTC แสดงแสดงโครงสร้างเพอรอฟสไกต์แบบผลึกเดี่ยวในตัวอย่าง LST และ $\text{La}_{0.3}\text{Sr}_{0.7}\text{Ti}_{0.9}\text{Co}_{0.10}\text{O}_{3.6}$ (LSTC_{0.10}) ในขณะที่ตัวอย่างอื่นๆพบการเกิดสารประกอบ La_2O_3 และ $\text{La}(\text{OH})_3$ จากนั้นทดสอบประสิทธิภาพของเซลล์อิเล็กโทรไลซิสแบบออกไซด์ของแข็งโดยมีอิเล็กโทรไลต์เป็นตัวรองรับของ $\text{La}_{0.3}\text{Sr}_{0.7}\text{Ti}_{1-y}\text{Co}_y\text{O}_{3.6}$ สำหรับการอิเล็กโทรไลซิสด้วยไอน้ำขั้วแคโทด LSTC ที่มีการเจือโคบอลต์ปริมาณ 10 เปอร์เซ็นต์โมลแสดงความหนาแน่นของกระแสสูงสุดที่ 800 °C เมื่อเทียบกับปริมาณการเจืออื่นๆ โดยมีความหนาแน่นกระแสเท่ากับ -1.08 A/cm^2 ที่ความต่างศักย์ 1.8 โวลต์ สำหรับอิเล็กโทรไลซิสระหว่างไอน้ำและคาร์บอนไดออกไซด์ (CO_2) และความทนทานต่อกํามะถัน LSTC_{0.10}/LSGM/Ag มีความหนาแน่นกระแสสูงสุดที่ 1.8 โวลต์ เช่นเดียวกัน (-0.91 A/cm^2) อย่างไรก็ตามความหนาแน่นกระแสลดลงเล็กน้อยเมื่อเปรียบเทียบกับกรอิเล็กโทรไลซิสด้วยไอน้ำ ในขณะที่ความต้านทานเฉพาะพื้นที่ (ASR) เพิ่มขึ้นเมื่อเพิ่ม CO_2 และ H_2S ในระบบและประสิทธิภาพทางเคมีไฟฟ้าลดลงในช่วงเวลาการทำงานเป็นเวลา 24 ชั่วโมง สำหรับ LST/LSGM/Ag ค่าความต้านทานเพิ่มขึ้นจาก 6.02 เป็น 8.50 $\Omega \times \text{cm}^2$ และ LSTC_{0.10}/LSGM/Ag ค่าความต้านทานเพิ่มขึ้นจาก 2.82 to 3.87 $\Omega \times \text{cm}^2$

สาขาวิชา วิศวกรรมเคมี
ปีการศึกษา 2565

ลายมือชื่อนิสิต
ลายมือชื่อ อ.ที่ปรึกษาหลัก

6370100021 : MAJOR CHEMICAL ENGINEERING

KEYWORD: LSTC Solid oxide electrolysis cell Intermediate temperature Hydrogen
electrode Sulfur tolerant

Natthamon Nuengjumnong : Sulfur-tolerant cobalt-doped $\text{La}_{0.3}\text{Sr}_{0.7}\text{TiO}_{3-d}$ -perovskite
cathode for intermediate-temperature solid oxide electrolysis cell. Advisor: Assoc.
Prof. PATTARAPORN KIM, Ph.D.

Lanthanum doped strontium titanate (LST) is a perovskite cathode in Solid Oxide Electrolysis Cell (SOEC) which shows great performance in syngas production from CO_2 and steam feed. However, the LST type cathode suffers from structural stability. Sulfur containing in industrial exhaust gas can affect its durability which inhibit the technology in real application. Therefore, to improve sulfur tolerance, $\text{La}_{0.3}\text{Sr}_{0.7}\text{Ti}_{1-y}\text{Co}_y\text{O}_{3-\delta}$ (LSTC) by adding Co^{2+} metal ion at B-site when y is 0 to 20%mol was synthesized. Citrate acid-nitrate combustion method was used and the synthesized powder. LST and $\text{La}_{0.3}\text{Sr}_{0.7}\text{Ti}_{0.9}\text{Co}_{0.10}\text{O}_{3-\delta}$ (LSTC_{0.10}) exhibited single phase perovskite while La_2O_3 and $\text{La}(\text{OH})_3$ were observed in other samples. The electrolyte-supported cell was then fabricated instead of the cathode support to test the performance of each $\text{La}_{0.3}\text{Sr}_{0.7}\text{Ti}_{1-y}\text{Co}_y\text{O}_{3-\delta}$. The cell with the LSTC_{0.10} cathode shows the highest current density at 800 °C compared to the other compositions. The current density was -1.08 A/cm^2 at operating voltage of 1.8 V for steam electrolysis. For steam/ CO_2 co-electrolysis and sulfur tolerance, The LSTC_{0.10}/LSGM/Ag produced the highest current density (-0.91 A/cm^2) at 1.8 V. However current density decreased slightly and the area specific resistance (ASR) increased when CO_2 and H_2S are added in feed. The electrochemical performance decreased for over operation time for 24 h. For LST/LSGM/Ag, the total polarization resistance increased from 6.02 to $8.50 \Omega\text{cm}^2$. And for LSTC_{0.10}/LSGM/Ag, the total polarization resistance increased from 2.82 to $3.87 \Omega\text{cm}^2$.

Field of Study: Chemical Engineering

Student's Signature

Academic Year: 2022

Advisor's Signature

ACKNOWLEDGEMENTS

I want to extend my sincere thanks to my assistant advisor Associate Professor Dr. Pattraporn Kim for her generosity, inspiration, and counsel. Her advice and encouragement were a helpful to me while I wrote my thesis and conducted my research. Additionally, CECC student for sharing their happiness and life advice. Also receiving my deepest gratitude are the professors, researchers, officials, and friends at Chulalongkorn University's college of chemical engineering. I want to genuinely thank my family for all of their love, inspiration, and encouragement throughout my life.

Natthamon Nuengjumnong



TABLE OF CONTENTS

	Page
.....	iii
ABSTRACT (THAI)	iii
.....	iv
ABSTRACT (ENGLISH)	iv
ACKNOWLEDGEMENTS	v
TABLE OF CONTENTS	vi
LIST OF FIGURES	vi
CHAPTER I INTRODUCTION.....	1
1.1 Background.....	1
1.2 Research objectives.....	3
1.3 Research scopes.....	3
1.4 Expected benefits	4
CHAPTER II THEORY AND LITERATURE REVIEWS	5
2.1 Hydrogen and syngas production.....	5
2.2 General principle of CO ₂ /H ₂ O co-electrolysis in solid oxide electrolysis cell.....	8
2.3 Perovskite oxide for solid oxide electrolysis cells	12
2.3.1 Structure of perovskite.....	12
2.3.2 The tolerance factor (t) in perovskite	14
2.3.3 Non-stoichiometric of perovskite	14
2.4 Key materials of SOECs for CO ₂ /H ₂ O co-electrolysis.....	15
2.4.1 Electrolyte materials.....	16

2.4.2 Anode materials.....	17
2.4.3 Cathode materials.....	17
2.5 Metal doping at B site of LST.....	20
2.5.1 Cr-doped LST.....	20
2.5.2 Mn-doped LST.....	22
2.5.3 Co-doped LST.....	23
2.6 Perovskite synthesis.....	26
2.6.1 Solid-state reaction.....	26
2.6.2 Co-precipitation.....	26
2.6.3 Citrate/nitrate combustion method.....	26
CHAPTER III EXPERIMENTAL.....	28
3.1 Chemicals and equipment.....	28
3.1.1 Chemicals.....	28
3.1.2 Tool and equipment.....	29
3.2 Synthesis of perovskite cathode powder by citrate/nitrate combustion method	30
3.3 Electrolyte-supported solid oxide electrolysis cell fabrication.....	31
3.4 Characterization of cathode perovskite.....	32
3.5 Electrochemical performance measurements.....	33
CHAPTER IV RESULTS AND DISCUSSION.....	36
4.1 Structural characterizations.....	36
4.2 Thermogravimetric analysis.....	40
4.3 X-ray photoelectron spectroscopy analysis.....	41
4.4 Calculation of tolerance factor (t).....	45

4.5 Electrochemical performance.....	46
CHAPTER V CONCLUSIONS.....	58
REFERENCES	60
APPENDIX.....	68
VITA.....	72



LIST OF FIGURES

Figure 2.1 The schematic drawing of co-electrolysis SOEC	9
Figure 2.2 Relationships between ΔH , DG, and DS of SOECs reactions for CO ₂	10
Figure 2.3 The relationship between ΔG and ΔH of the WGS reaction	11
Figure 2.4 Simple structure of ABO ₃ perovskite compounds	13
Figure 2.5 Schematic representation of triple phase boundaries in SOFCs	16
Figure 2.6 Temperature dependence of electrical conductivity of La _{0.3} Sr _{0.7} Ti _{1-x} Cr _x O _{3-δ} (x= 0, 0.1, 0.2).	21
Figure 2.7 Electrical conductivity of La _{0.3} Sr _{0.7} Ti _{1-x} Cr _x O _{3-δ} samples at 800°C in alternative atmospheres (air and 5% H ₂ /Ar) (a) x= 0 and (b) x= 0.2.....	21
Figure 2.8 Variation of electrical conductivities of La _{0.6} Sr _{0.4} Ti _{1-x} Mn _x O _{3-δ} in humidified H ₂ (97% H ₂ + 3% H ₂ O).	22
Figure 2.9 Comparison of the I-V curves and power densities of the La _{0.6} Sr _{0.4} Ti _{1-x} Mn _x O _{3-δ} at 800°C.....	23
Figure 2.10 Maximum power density of the cells with different fuels: (a) pure H ₂ and (b) 5000 ppm H ₂ S-H ₂ at different temperatures.....	24
Figure 2.11 Long-term stability test of the LSCT-based cell at 400 mA·cm ⁻² and 900°C in humid 5000 ppm H ₂ S-H ₂ feed.	25
Figure 2.12 Maximum power density of the LSCT-based cell as a function of time at 850°C with H ₂ fuel after each redox cycle.	25
Figure 3.1 The conditions of calcination for LSTC perovskite anode	31
Figure 3.2 Schematic drawing of the electrolyte-supported cell.....	32
Figure 3.3 Equivalent circuit for impedance response fitting	34
Figure 3.4 Schematic drawing of the test system.....	35
Figure 4.1 XRD patterns of La _{0.3} Sr _{0.7} Ti _{1-y} Co _y O _{3-δ} (LSTC) where y = 0, 0.05, 0.1, 0.15 and 0.2: a) after sintered in air at 1200°C for 2 h; and b) magnified scale at 2θ angles between 31° and 34°	37

Figure 4.2 SEM images of $\text{La}_{0.3}\text{Sr}_{0.7}\text{Ti}_{1-y}\text{Co}_y\text{O}_{3-\delta}$ (LSTC) sintered at 1200°C for 2 h: (a) LST, (b) $\text{LSTC}_{0.05}$, (c) $\text{LSTC}_{0.10}$, (d) $\text{LSTC}_{0.15}$, and (e) $\text{LSTC}_{0.20}$	39
Figure 4.3 EDX images of $\text{La}_{0.3}\text{Sr}_{0.7}\text{Ti}_{1-y}\text{Co}_y\text{O}_{3-\delta}$ (LSTC) find powder where $y = 0, 0.05, 0.1, 0.15$ and 0.2 which sintered at 1200°C for 2 h.	39
Figure 4.4 TGA profile of $\text{La}_{0.3}\text{Sr}_{0.7}\text{Ti}_{1-y}\text{Co}_y\text{O}_{3-\delta}$ (LSTC) find powder where $y = 0, 0.05, 0.1, 0.15$ and 0.2 which sintered at 1200°C for 2 h in air at room temperature to 800°C.....	41
Figure 4.5 Low resolution XPS spectra of $\text{La}_{0.3}\text{Sr}_{0.7}\text{Ti}_{1-y}\text{Co}_y\text{O}_{3-\delta}$ (LSTC) ($0 \leq y \leq 0.2$) powder.....	42
Figure 4.6 The deconvoluted of XPS spectra of $\text{La}_{0.3}\text{Sr}_{0.7}\text{Ti}_{1-y}\text{Co}_y\text{O}_{3-\delta}$ (LSTC) ($0 \leq y \leq 0.2$) powder: (a) O 1s, and (b) Ti 2p	43
Figure 4.7 The deconvoluted of Co 2p XPS spectra of $\text{La}_{0.3}\text{Sr}_{0.7}\text{Ti}_{1-y}\text{Co}_y\text{O}_{3-\delta}$ (LSTC) ($0 \leq y \leq 0.2$) powder.....	45
Figure 4.8 Tolerance factor of $\text{La}_{0.3}\text{Sr}_{0.7}\text{Ti}_{1-y}\text{Co}_y\text{O}_{3-\delta}$ (LSTC) ($0 \leq y \leq 0.2$) powder at room temperature.....	46
Figure 4.9 Comparison of the electrochemical performance of various operating temperature and C1 (50% H_2O , 6.67% H_2) feed composition: a) LST, b) $\text{LSTC}_{0.05}$, c) $\text{LSTC}_{0.1}$, d) $\text{LSTC}_{0.15}$, and e) $\text{LSTC}_{0.2}$	48
Figure 4.10 Comparison of the electrochemical performance of various Co contents from 0 to 20%mol and the feed composition was controlled at a constant C1 (50% H_2O , 6.67% H_2) at 800°C: (a) IV profiles, and (b) electrochemical impedance response (EIS)	49
Figure 4.11 Comparison of the electrochemical performance of various feed composition at 800°C: (a-e) electrolyte-supported of $\text{La}_{0.3}\text{Sr}_{0.7}\text{Ti}_{1-y}\text{Co}_y\text{O}_{3-\delta}$ (LSTC) with varying Co contents from 0 to 20%mol, respectively	52

- Figure 4.12** Comparison of the electrochemical performance at 800°C: (a) IV profiles, of various Co contents from 0 to 20%mol and the feed composition was controlled at a constant C6 (15 ppm H₂S), and (b) electrochemical impedance response (EIS) of LSTC_{0.10}/LSGM/Ag with various feed compositions 54
- Figure 4.13** Comparison of LST/LSGM/Ag electrochemical impedance response at different duration (800 °C with C6 feed composition for 24 h).....56
- Figure 4.14** Comparison of LSTC_{0.10}/LSGM/Ag electrochemical impedance response at different duration (800 °C with C6 feed composition for 24 h) 56
- Figure A.1** XRD pattern of LST.....68



LIST OF TABLES

Table 2.1 Processing Options for hydrogen and syngas production in terms of hydrogen source, energy source, and chemical reaction processes	7
Table 3.1 The compositions of cathode	30
Table 3.2 Flow rate of each flue gas component for SOEC electrolysis.....	34
Table 4.1 The lattice parameters and lattice volumes of $\text{La}_{0.3}\text{Sr}_{0.7}\text{Ti}_{1-y}\text{Co}_y\text{O}_{3-\delta}$ (LSTC)	38
Table 4.2 The stoichiometry of $\text{La}_{0.3}\text{Sr}_{0.7}\text{Ti}_{1-y}\text{Co}_y\text{O}_{3-\delta}$ where $y = 0, 0.05, 0.1, 0.15$ and 0.2 which sintered at 1200°C for 2 h calculated from EDX analysis.....	40
Table 4.3 The $\text{O}_{\text{adsorbed}}/\text{O}_{\text{lattice}}$ ratio for various cobalt contents.....	43
Table 4.4 The $\text{Ti}^{3+}/\text{Ti}^{4+}$ ratio for various cobalt contents.....	44
Table 4.5 Resistance of the various electrolyte support LSTC/LSGM/Ag of various Co contents from 0 to 20%mol and the feed composition was controlled at a constant C1 ($50\%\text{H}_2\text{O}$, $6.67\%\text{H}_2$) at 800°C . R_{Ohmic} , R_{HF} and R_{LF} are referred to ohmic resistance and polarization resistance in high frequency region and low frequency region, respectively.....	51
Table 4.6 Resistance of the various feed composition of $\text{LSTC}_{0.10}/\text{LSGM}/\text{Ag}$ at 800°C . R_{Ohmic} , R_{HF} and R_{LF} are referred to ohmic resistance and polarization resistance in high frequency region and low frequency region R_{T} are total resistance, respectively.....	55
Table 4.7 Resistance of LST/LSGM/Ag and $\text{LSTC}_{0.10}/\text{LSGM}/\text{Ag}$ at 800°C with C6 feed composition for 24 h. R_{Ohmic} , R_{HF} and R_{LF} are referred to ohmic resistance and polarization resistance in high frequency region and low frequency region R_{T} are total resistance, respectively	57
Table C.1 Ionic charge, coordination number and ionic radius of concerned metals	71

CHAPTER I

INTRODUCTION

1.1 Background

Nowadays, the global economy is expanding faster. As a reason, the energy demand is constantly increasing, resulting in extravagant use of natural resources. Natural resources are used to produce fuels such as oil, natural gas, coal, and others. As a result, natural resources are limited and tend to exhaust rapidly, and nonrenewable.

Hydrogen (H_2) and syngas (a fuel gas mixture made up of hydrogen and carbon monoxide (CO)) can be used as an intermediate in the production of synthetic natural gas (SNG), ammonia, methanol and etc. Hydrogen and syngas are alternative fuels that are efficient energy carriers for renewable energy. Hydrogen and syngas can be produced from a variety of any hydrocarbon feedstock consisting of natural gas, coal, biomass, residual oil, or solid waste. Most of the global production uses steam reforming, dry reforming, or partial oxidation, gasification, chemical looping and reduction [1] However, the process generates greenhouse gas emission which is a significant contributor to global warming. The key priorities for increasing Thailand's energy security are low-cost energy production technology and environmental sustainability. Hydrogen and syngas production methods must use energy more effectively, provide ultraclean fuels, remove pollutant emissions at end-use systems, Hence, electrochemical technologies such as solid oxide electrolysis cells (SOEC) have attracted considerable attention.

The solid oxide electrolysis cells consist of cathode, electrolyte and anode. Carbon dioxide, steam (H_2O), and steam/carbon dioxide can be electrolyzed in oxygen-ion conducting solid oxide electrolysis cells to produce carbon monoxide,

hydrogen, and syngas, respectively. Solid oxide electrolysis cells usually operate as high-temperature solid oxide electrolysis cells (HT-SOECs). Following thermodynamic principles, raising temperature leads to lower power requirements despite rising heat energy demand [2-5]. External waste heat sources can be utilized, reducing H_2 production cost. The operating temperature of high-temperature solid oxide electrolysis cells was in the range of 700-1000°C. Nickel (Ni)-based cathodes were often used as hydrogen electrodes. However, they are also not resistant to sulfur compounds, such as hydrogen sulfide (H_2S), which are commonly found in the emissions from fossil fuel power plants and steel-making blast furnaces. At high temperatures, materials are subjected to not only internal thermal stresses, but also external thermal stresses at the electrode-electrolyte interface. Promoting diffusion kinetics may cause changes in the chemistry of surrounding portions and thermal expansion, leading the solid oxide electrolysis cells to degrade. Materials which are able to tolerate high temperatures are required [6]. Otherwise, materials which operated at lower temperature while maintaining high performance should be developed [7]. The development of materials for solid oxide electrolysis cells in the intermediate temperature range, as well as improving the cell's performance to sulfur tolerance and durability, remains a challenge.

Perovskite is an interesting material for intermediate-temperature solid oxide electrolysis cells (IT-SOECs) cathode materials since it solves the issue of nickel surface carbon crystallization. These materials also have a mixed conductivity property, allowing for a wider electrochemical response of ionic and electronic conductivity. This is due to a triple-phase boundaries (TPBs) that runs across the anode. lanthanum doped strontium titanate (La doped $SrTiO_3$, LST) is an intriguing cathode material since it is stable in typical atmospheric conditions, has high conductivity, and can function at intermediate temperatures. Although LST has a greater conductivity, it has a worse phase and chemical stability. Ionic conductivity, electro catalytic activity, surface rearrangement segregation are main drawbacks of the

LST cathode materials. Doping LST on B-site with other metal ions and adding an active second phase to LST to produce a composite cathode are currently the two major approaches for enhancing ionic conductivity and improving fuel cell performance. In recent years, LST-based materials doped with various transition metal elements such as chromium (Cr), iron (Fe), and Cobalt (Co) in the B-site have been studied. On the oxidation–reduction process, transition metal catalytic activities are well known to follow the order $\text{Co} > \text{Fe} > \text{Cr}$. Co^{2+} is an interesting additional metal to LST [8, 9].

In this study, the effect of cobalt content in the B-site of LST was investigated for use in $\text{CO}_2/\text{H}_2\text{O}$ -fed intermediate-temperature solid oxide electrolysis cell. Sulfur tolerance and electrochemical performance of the electrode were investigated.

1.2 Research objectives

To prepare $\text{La}_{0.3}\text{Sr}_{0.7}\text{Ti}_{1-y}\text{Co}_y\text{O}_{3-\delta}$ (LSTC) and investigate electrochemical performance and sulfur tolerance toward $\text{CO}_2/\text{H}_2\text{O}$ electrolysis at intermediate temperature.

Subobjective includes:

1.2.1 To synthesize $\text{La}_{0.3}\text{Sr}_{0.7}\text{Ti}_{1-y}\text{Co}_y\text{O}_{3-\delta}$ (LSTC) with partial substitution of LST on B-site with Co^{+2} .

1.2.2 To investigate the effect of the amounts of Co^{+2} dopant on the electrochemical performance and sulfur tolerance of the perovskite cathode.

1.3 Research scopes

- Single phase perovskites of $\text{La}_{0.3}\text{Sr}_{0.7}\text{Ti}_{1-y}\text{Co}_y\text{O}_{3-\delta}$ ($y = 0, 5, 10, 15$ and 20%mol) are synthesized by citrate/nitrate combustion method.
- The conductivity and thermal expansion study temperature are ranged from 600-800°C.
- For electrolyte-supported cell, $\text{La}_{0.8}\text{Sr}_{0.2}\text{Ga}_{0.8}\text{Mg}_{0.3}\text{O}_3$ (LSGM) and silver (Ag) are used for electrolyte and anode layer, respectively.

- The cell are fabricated by mold and press, and Doctor blade technique.
- Cathode feed compositions include H_2O (50% and 67%), CO_2 (10% and 17%), and sulfur (10 and 15 ppm)
- Co^{+2} dopant concentration is varied from 0 to 0.2 mol% in the perovskite.

1.4 Expected benefits

From this research, it is expected that SOEC can operate at intermediate temperature with CO_2 and sulfur containing feed. Sulfur tolerance of the electrode can be improved.



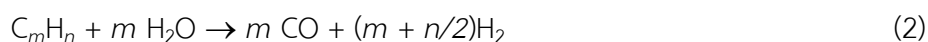
CHAPTER II

THEORY AND LITERATURE REVIEWS

2.1 Hydrogen and syngas production

In chemical industries such as oil refining, ammonia production, dimethyl ether, methanol, and aniline production, hydrogen is a key raw material. It also has the potential as fuel due to advantages like stability, renewability, high energy content, ease of storage and transportation, high efficiency, and environmental responsibility. In addition to hydrogen, synthesis gas (hydrogen and carbon monoxide) performs an important role as an intermediate in industry. Syngas can be utilized to make methanol, Fischer–Tropsch fuels, ethanol, and dimethyl ether, among other chemicals and fuels [10]. At present, syngas and hydrogen production can be defined in a variety of methods. Steam reforming, partial oxidation, auto thermal reforming, and oxidative steam reforming can be commonly used. The equations below show the different reactions in four different processing phases utilizing four different fuels: liquid hydrocarbon fuels (C_mH_n), methanol (CH_3OH , $MeOH$), or several alcohols for mobile applications, natural gas (CH_4) and liquefied propane gas (LPG) for industrial applications, and coal gasification for large-scale industrial applications. The majority of reactions (Eqs. 1–7) necessitate certain catalysts and process conditions. Some reactions (Eqs. 8–11) are undesirable, and they can happen in specific circumstances.

- Steam reforming



- Partial oxidation



- Carbon formation



From the above-mentioned process, in the gaseous mixture, there are by-product gases such as CO, CO₂, H₂S, and etc. Furthermore, as indicated in Table 2.1, hydrogen can be produced using a variety of methods and sources. Hydrogen production development is a research challenge in the environmental and energy research sector, as it seeks to improve processes while minimizing environmental effects and energy usage.

Table 2.1 Processing Options for hydrogen and syngas production in terms of hydrogen source, energy source, and chemical reaction processes [10]

Hydrogen Source	Energy Source	Reaction Processes
1. Fossil hydrocarbons Natural gas ^a Petroleum ^b Coal ^{a,b} Tar sands, oil shale Natural gas hydrate 2. Biomass 3. Water 4. Organic/animal waste 5. Synthetic fuels MeOH, FTS liquids, etc. 6. Specialty areas Organics compound Metal hydride, chemical complex hydride Ammonia, hydrazine Hydrogen sulfide 7. Others	1. Primary Fossil energy ^c Biomass Organic waste Nuclear energy Solar energy Photovoltaic Hydropower Wind, wave, geothermal 2. Secondary Electricity H ₂ , MeOH, etc. 3. Special cases Metal bonding energy Chemical bonding energy 4. Others	1. Commercialized process Steam reforming ^d Autothermal reforming ^d Partial oxidation ^d Catalytic dehydrogenation ^e Gasification ^d Carbonization ^d Electrolysis ^f 2. Emerging approaches Membrane reactors Plasma reforming Photocatalytic Solar thermal chemical Solar thermal catalytic Biologic Thermochemical cycling Electrocatalytic 3. Others

^a Currently used hydrogen sources for hydrogen production.

^b Currently used in chemical processing that produces H₂ as a by - product or main product.

^c Currently used as main energy source.

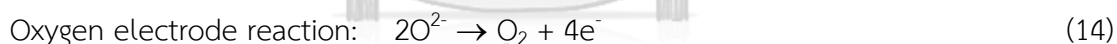
^d Currently used for syngas production in conjunction with catalytic water - gas shift reaction for H₂ production.

^e As a part of industrial naphtha reforming over Pt-based catalyst that produces aromatics.

^f Electrolysis is currently used in a much smaller scale compared with steam reforming.

2.2 General principle of CO₂/H₂O co-electrolysis in solid oxide electrolysis cell

The co-electrolysis of CO₂ and H₂O into valuable chemicals using high-temperature solid oxide electrolysis cells has lately gained interest owing to the high conversion and energy efficiency, which gives prospects for lowering CO₂ emissions and mitigating global warming. The single SOEC consists of three parts, hydrogen electrode (cathode), oxygen electrode (anode), and electrolyte where the co-electrolysis reaction takes place. The schematic drawing of SOEC is shown in Fig. 2.1. CO₂ and H₂O flow together into the porous cathode, where they both take electrons from external electricity to convert into CO, H₂, and O²⁻ ions on the cathode, and then the O²⁻ ion are transported through the electrolyte to evolve as O₂ on the anode and generate electron as shown in Eqs. 12-15.



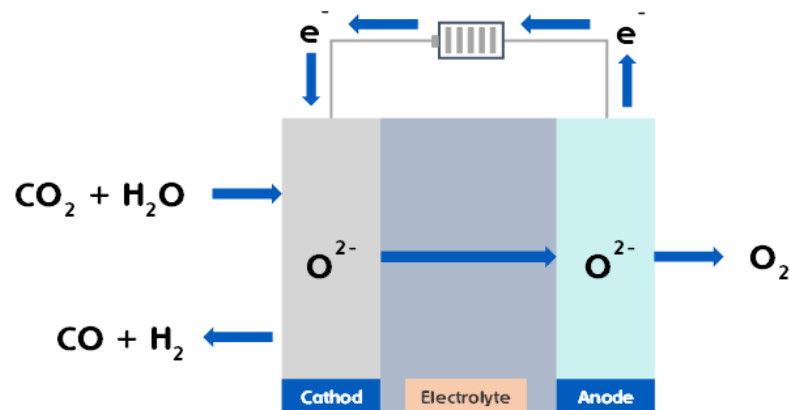


Figure 2.1 The schematic drawing of co-electrolysis SOEC

SOECs typically operate at high temperatures ($>800\text{ }^{\circ}\text{C}$) to decrease ohmic resistance due to the conductivity of electrolytes. The overall reaction of $\text{CO}_2/\text{H}_2\text{O}$ co-electrolysis is Eqs. 16, and the energy requirement is the reaction's enthalpy change (ΔH). In a term of Eqs. 17, the enthalpy change is formed of Gibbs free energy change (ΔG) and entropy change ($T\Delta S$), where the former ΔG and the latter $T\Delta S$ describe the electrical energy and heat energy that is required of SOEC for $\text{CO}_2/\text{H}_2\text{O}$ co-electrolysis, respectively. Eqs. 18 is obtained when these values are substituted into Eqs 17.



$$\Delta H = \Delta G + T\Delta S \quad (17)$$

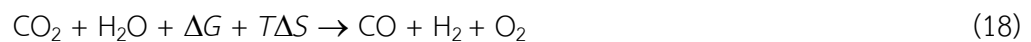


Fig. 2.2 demonstrates the transformation of total energy, electricity, and heat energy as the SOEC working temperature increases [11]. The total energy demanded is only slightly impacted by increasing the working temperature, as shown in Fig. 2.2, although the electricity energy demanded for $\text{CO}_2/\text{H}_2\text{O}$ co-electrolysis gradually decreases while the heat energy required for electrolysis increases. This

demonstrates that $\text{CO}_2/\text{H}_2\text{O}$ co-electrolysis employing HT-SOECs might benefit from thermodynamics, as heat energy is significantly cheaper than electricity.

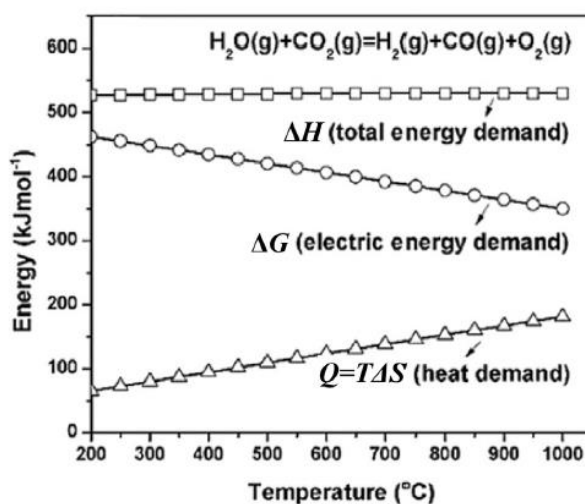


Figure 2.2 Relationships between ΔH , ΔG , and $Q=TS$ of SOECs reactions for CO_2 [11]

Co-electrolysis is more difficult than separate electrolysis processes of H_2O and CO_2 because of the water gas shift (WGS) reaction in which H_2O is decreased in the forward reaction and CO_2 is reduced in the reverse reaction (reverse water gas shift, RWGS) as shown in Eqs. 19. In Fig. 2.3, the ΔH and ΔG values of the WGS reaction are presented as a function of temperature. The curves drop rapidly at 100°C due to a phase shift from a liquid to a gaseous state. Additionally, the ΔG value of the WGS is 0 at 816°C , showing that the forward reaction is more favorable at lower temperatures ($\Delta G < 0$), whereas the reverse process is the opposite. When the temperature increases exceeding 3000°C , the CO_2 electrolysis process becomes spontaneous, but the material's stability suffers. However, operations at $600\text{--}1000^\circ\text{C}$ with a gas feed stream are significantly simpler than operations at room temperature with liquid/gas feeds [12]. As can be seen, the cell layouts and material requirements for high-temperature electrolysis systems are different from those for low-

temperature electrolysis systems. Finally, through Eqs. 21, the presence of steam can significantly relieve carbon deposition (Eqs. 20, at greater overpotential).

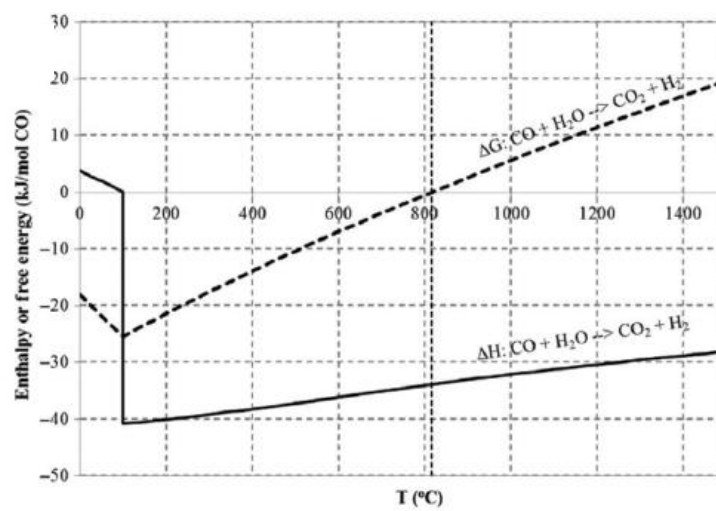


Figure 2.3 The relationship between ΔG and ΔH of the WGS reaction [12]

At present, there seems to be a significant focus on intermediate-temperature solid oxide fuel cells (IT-SOFCs), which generally operate between 600 and 800°C, to allow for a broader materials selection, more cost-effective SOFC manufacture, increased durability [13]. As in SOEC, when the operating temperature is reduced, several heat sources from industrial plants, such as steel-making plants or other combustors, can also be used for SOEC. At present, SOEC is currently a very appealing energy recovery method for unused heat energy. As a reason, the development of an intermediate-temperature solid oxide electrolysis cells is urgently needed in order to maximize energy efficiency.

2.3 Perovskite oxide for solid oxide electrolysis cells

Several innovative SOFCs/SOECs with various topologies have been created in recent years, including single-layer SOFCs/SOECs [14, 15], electrolyte layer-free SOFCs [16], and all-in-one SOFCs/SOECs [17, 18]. Nevertheless, the thermal deterioration of materials under high-temperature working settings (850-1000°C) limits the commercialization of traditional SOECs. As a result, one of the major problems of current SOEC technologies is the creation of SOEC that can function at lower temperatures via steam and carbon dioxide co-electrolysis including hydrogen sulfide impurities in parts per million (ppm) amounts in the cathode of SOECs. Traditional Ni-based electrode of catalysts have excellent electrochemical activity and electrical conductivity in a reducing environment, but they have disadvantages. These disadvantages can be found in SOFCs/SOECs include Ni aggregation and coarsening over long-term operation [19], carbon deposition and performance degradation at intermediate temperatures [20, 21], sulfur poisoning causes cathode pores to be blocked by sulfur-containing chemicals, resulting in increased cathode polarization, shorter cathode lifetime, and the possibility of anode re-oxidation destruction [22, 23]. Desulfurization and/or reforming units must be added to the current SOFCs/SOECs system to tackle this problem. The development of novel, alternative electrode materials, structures, and/or methods that can solve these problems while demonstrating equivalent performance to present Ni-based electrode catalysts is of interest.

2.3.1 Structure of perovskite

Perovskite oxide is one of the most fundamental types of materials that have been widely applied as cathode, electrode, and anode components of SOECs. Perovskite oxide has a simple structure formula ABO_3 shown in Fig. 2.4, with the maximal sum of the oxidation states of the A-site and B-site cations being +6. The A-site and B-site are cation metals with different ion radius sizes [24]. The A-site

cation has a larger ion radius than the B-site cation and is found in the lattice's corner, whereas the B-site cation is found in the lattice's center. Strontium (II) ion (Sr^{2+}), barium (II) ion (Ba^{2+}), Lead (II) ion (Pb^{2+}), and Lanthanum (III) ion (La^{3+}) are examples of alkaline earth or rare-earth elements of A-site cation, while the B-site cation is a 3d, 4d, or 5d transition metal element [8]. Because of its combined ionic and electronic conductivity, structural stability, and little or no interaction with other cell components, perovskite compounds are widely used as electrodes in SOECs [25]. The oxide cathode based on perovskite is stable within a wide range of oxygen partial pressures in both oxidizing and reducing conditions [26]. Furthermore, the chemical composition, preparation procedure, sintering temperature, and atmosphere employed in the studies all have a significant impact on its conductivity. The major cause of perovskite oxide degradation is surface rearrangement, which can be caused by the electrode composition's solubility limit or external factors such as feed gas impurity, operating temperature, oxygen partial pressure, and electric field [8].

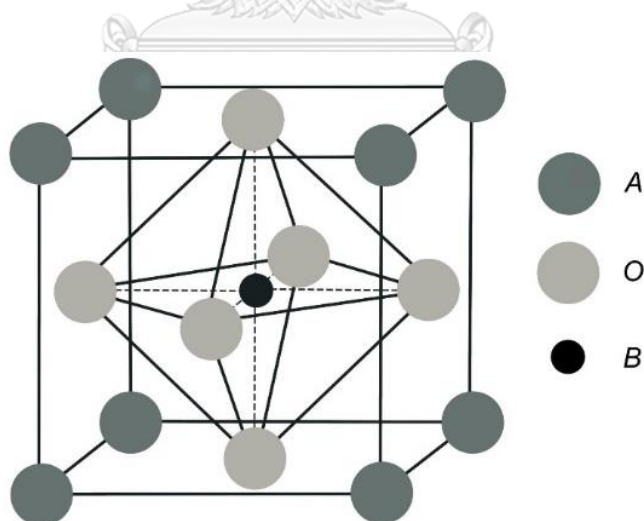


Figure 2.4 Simple structure of ABO_3 perovskite compounds [27]

2.3.2 The tolerance factor (t) in perovskite

To calculate the stability of the perovskite phase for a given combination of anions and cations, use the tolerance factor (t). The tolerance factor is a set of characteristics connected to perovskites' symmetry that have a substantial impact on their dielectric properties. As shown in Fig. 2.4, in order for the A, B, and O ions to make contact, $r_A + r_O$ must equal $\sqrt{2}(r_B + r_O)$, where r_A , r_B , and r_O are the ionic radii of the A-site cation, B-site cation and oxygen ion, respectively. The tolerance factor in perovskite lattice follows the relationship as shown in Eqs. 22

$$t = \frac{r_A + r_O}{\sqrt{2}(r_B + r_O)} \quad (22)$$

A cubic structure is formed when t is near to 1. Nevertheless, when t is less than 0.9 or more than 1, perovskite oxide shows pseudo-symmetry, where the cubic lattice made up of arrays of corner-sharing BO_6 octahedral tilted to orthorhombic or hexagonal lattice. The ability to construct diverse perovskite oxide compositions and structures with varying characteristics is one of the most appealing aspects of perovskite oxide [28].

2.3.3 Non-stoichiometric of perovskite

Non-stoichiometric compounds are chemical compounds that have deviated from stoichiometry and cannot be represented by a natural number ratio. The majority of non-stoichiometric compounds are transition metal oxides, which are a component of the B-site in the general formula, $\text{ABO}_{3-\delta}$ in the perovskite structure. Non-stoichiometry in perovskites is generally caused by oxygen deficit ($\text{ABO}_{3-\delta}$), cation insufficiency at the A-site ($\text{A}_{1-\delta}\text{BO}_3$), or cation deficiency at the B-site ($\text{AB}_{1-\delta}\text{O}_3$). The size and coordination number of A and B cations are significant to oxygen deficiency. Replacement of ions of the same magnitude but different valence is used to fill oxygen vacancies. When La^{3+} in LaBO_3 is replaced with Sr^{2+} to make $\text{La}_{1-x}\text{Sr}_x\text{BO}_{3-\delta}$, oxygen vacancies are created in the structure. Because the arrangement in BO_3

makes a very suitable network for stability purposes, A-site cations may be partially absent, although B-site vacancies are rare due to the high cation, which leads to the small size [29].

2.4 Key materials of SOECs for CO₂/H₂O co-electrolysis

CO₂/H₂O co-electrolysis in SOECs needs rigorous cathode requirements because of the high reaction temperature, complicated reactions, and unique redox conditions: (1) keeping the temperature stable from ambient temperature to the operating temperature of the SOEC; (2) for mass transfer, a porous structure is used; (3) during the manufacturing and operation of the electrolyte, it must be thermally and chemically compatible; (4) sufficient electrical conductivity in a redox environment; (5) for electro-reduction of CO₂ and H₂O, it has a high electro-catalytic activity. Accordingly, since electro-reduction of CO₂ and H₂O reactions occur on the cathode's surface, as shown in Fig. 2.1, greater attention should be directed to the cathode and associated processes. As a result, a large number of studies have been devoted to the development of cathode materials to effectively convert CO₂ and H₂O. Co-electrolysis of CO₂ and H₂O occurs on the cathode of SOECs at the points where the catalyst, ionic conductor, electronic conductor, and gas phase are in contact. The triple phase boundaries (TPBs) of the electronic conductor, ionic conductor, and gas are the real active sites for CO₂/H₂O co-electrolysis since the electronic conductor is utilized as the catalyst in most situations. As a result, the high-performance cathode must have higher TPBs for CO₂/H₂O co-electrolysis. The schematic representation of TPBs can be seen on Fig. 2.5.

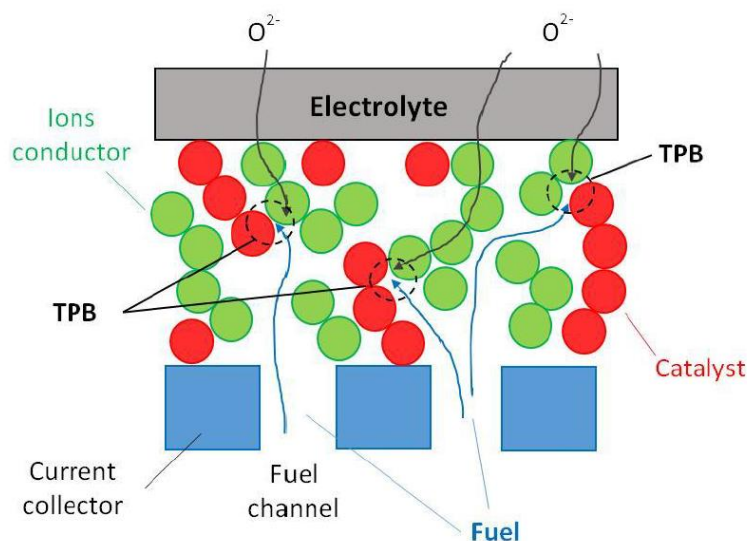


Figure 2.5 Schematic representation of triple phase boundaries in SOFCs [30]

The majority of functional perovskite oxides used in SOECs have high oxygen ionic and electronic conductivities at the same time, a property known as mixed ionic-electronic conducting (MIEC). MIEC perovskite exhibits substantially greater regions of triple-phase boundaries, i.e., interfacial contact areas between oxygen ions, oxygen gases, and electrons, than typical electronic conducting or ionic conducting perovskite.

จุฬาลงกรณ์มหาวิทยาลัย
CHULALONGKORN UNIVERSITY

2.4.1 Electrolyte materials

The electrolyte layer in oxygen ion-conducting SOECs conducts oxygen ions from the cathode to the anode. To achieve a high-power output, the electrolyte materials should have a high ionic conductivity at their operating temperature. Furthermore, because the electrolyte layer is sandwiched between the anode and the cathode, which are exposed to oxidizing and reducing atmospheres, the electrolyte material must be densely sintered and mechanically and chemically stable. Conduction of oxygen ions in a dense solid material is generally influenced by lattice defects and driven by a concentration gradient or current. Perovskite-based

oxides, such as $\text{La}_{0.8}\text{Sr}_{0.2}\text{Ga}_{0.8}\text{Mg}_{0.3}\text{O}_3$ (LSGM), are also essential oxygen ion electrolytes in IT-SOECs. This type of material has been the focus of numerous investigations in the past. Among the $\text{La}_{1-x}\text{Sr}_x\text{Ga}_{1-y}\text{Mg}_y\text{O}_{3.8}$ ($x=0.10\text{--}0.20$ and $y=0.15\text{--}0.20$) series oxide electrolytes, LSGM has greater ionic conductivity at intermediate temperatures than stabilized zirconia (ZrO_2) and higher ion transfer numbers than doped ceria (CeO_2) [31]. At 600°C , the sintered sample had a relative density of 98% and a total conductivity of $1.13 \times 10^{-2} \text{ S}\cdot\text{cm}^{-1}$ after being synthesized using a co-precipitation route in an aqueous medium [32]. Therefore, LSGM is particularly appealing as an electrolyte in IT-SOECs.

2.4.2 Anode materials

As the best catalysts for the oxygen reduction process (ORR) at low temperatures, Platinum (Pt) or Pt-alloys were utilized in the majority of the reported IT-SOFCs with high power output. However, Pt is a costly noble metal with a relatively limited global resource. The high cost and scarcity of Pt is seen as a major impediment to the commercialization of IT-SOFCs. When silver (Ag), electrolyte, and oxygen gas are physically in contact, ORR on Ag can occur either at the triple phase boundary (TPB) or over the whole surface of Ag when it functions as a mixed ion-electron conducting (MIEC) electrode [33].

2.4.3 Cathode materials

Cathodes, or fuel electrodes, can work properly as reaction active sites for reactants such H_2O and CO_2 . Ni-YSZ is the most commonly studied and used fuel electrode in SOECs. Cause of its high electrocatalytic activity, affordable cost, and operational dependability in with networks of Ni, YSZ, and pores acting as transport channels for electrons, ions, and gases, respectively. Apart from this, long-term stability problems such as particle aggregation, carbon deposition, Ni oxidation, sulfur poisoning, and SiO_2 poisoning. As a result, innovative materials must be created to

solve these concerns. Many mixed perovskite oxides are now in use, including chromite-based perovskites and strontium titanate (ST)-based perovskites and lanthanum (La) doped to SrTiO_3 (LST)-based perovskites, which are discussed below.

Over the last decade, several investigations have been conducted to investigate the applicability of strontium doped lanthanum chromite (LSCr) single perovskites as SOECs cathode materials. Because Cr possesses strong hexagonal coordination with oxygen deficiency [34], the addition of cations with a lower coordination number (e.g. Co, Fe, and Ni) can improve the catalytic activity of LSCr [35]. At reducing atmospheres with temperature increased, the presence of these cations in the B-site can cause oxygen vacancies, leading to increased LSCr cathode electrical conductivity. The oxygen-deficient perovskite i.e., $\text{La}_{0.75}\text{Sr}_{0.25}\text{Cr}_{0.5}\text{Mn}_{0.5}\text{O}_{3.8}$ (LSCM) is a hydrogen electrode for SOECs. These materials compare favorably to typical Ni/YSZ cermet in terms of electrochemical performance and catalytic activity at high temperatures. At 900°C of SOFCs, the polarization resistance (R_p) of LSCM in 3% $\text{H}_2\text{O}/97\%\text{H}_2$ is determined to be $0.2 \Omega\text{cm}^2$ [36]. However, two disadvantages of LSCM material have been identified: its poor electrical conductivity in reducing atmosphere compared to Ni-YSZ ceramic and its inability to withstand the poisoning of sulfur impurities in the feedstock.

Single perovskites based on strontium titanate are stable throughout a wide range of oxygen partial pressures under oxidizing and reducing environments [26]. Furthermore, it is very resistant to carbon and sulfur deposition. Nonetheless, the conductivity and catalytic activity of pure- SrTiO_3 cathodes are lower, leading to higher R_p and lower power density values. It also possesses n-type semiconductor properties and a wide variety of applications. Because of their electrical conductivity and structural stability in reducing environments, N-type mixed conducting oxides are chosen as cathode materials over p-type conductors, as shown in Eqs 23.



Whereas, $\text{Ti}_{\text{Ti}}^{\times}$ = tetravalent B-site ion, $\text{Ti}_{\text{Ti}}^{\bullet}$ = trivalent ion, $\text{O}_{\text{O}}^{\times}$ = lattice oxygen $\text{V}_{\text{O}}^{\bullet\bullet}$ = oxygen vacancies.

Several methods for increasing perovskite conductivity were investigated, including substituting Ti^{4+} on the B-site with Sr^{2+} on the A-site. It entails the creation of oxygen, which contains sub-stoichiometric molecules that affect the final characteristics of the product. Furthermore, the A-site typically contains sodium (Na), potassium (K), and rare earth elements, whereas the B-site has chromium (Cr), iron (Fe), Manganese (Mn), and Cobalt (Co) [8, 9, 24, 37]. Lanthanum doped to SrTiO_3 at A-site can improve conductivity and oxygen stoichiometry by reducing Ti^{4+} to Ti^{3+} . LST showed reasonable chemical and thermal stability for SOFCs in reducing environment even in the presence of H_2S fuel.

One of the most common cathode choices among perovskite materials is lanthanum strontium titanate. The proportionate reduction of Ti^{4+} to Ti^{3+} caused by partial substitution of Sr^{2+} with La^{3+} often increases electronic conductivity. Even in the presence of H_2S , LST demonstrated reasonable thermal and chemical stability in SOFCs anode environment [38]. However, its lower catalytic activity for fuel oxidation processes resulted in low maximum power densities for LST anode-based single cells of $35 \text{ mW}\cdot\text{cm}^{-2}$ in H_2 and $1.6 \text{ mW}\cdot\text{cm}^{-2}$ in CH_4 at 800°C [39], rendering it unsuitable for industrial application. La has a maximum solubility of 0.6 in SrTiO_3 . However, in $\text{La}_x\text{Sr}_{1-x}\text{TiO}_3$, the usual x is 0.3 or 0.4. When x exceeds 0.5, the structure will be distorted [9]. The following are some of the current ways being used to improve LST properties:

- (a) Doping other metal cations into the La and Ti lattices.
- (b) Surface precipitation of nano-structured particles after pre-reduction of doped LST in a strong reducing environment.
- (c) Composite materials including an ionic conducting phase of O_2 and LST.

Sinter ability, structure, redox characteristics, conductivity, and electrocatalytic efficacy of LST molecules are all influenced by the type of A/B-site dopants [40]. Appropriate doping elements can affect the number of titanium mixed-oxidation state Ti^{4+}/Ti^{3+} and oxygen vacancies. Some catalytically active materials are dissolved in the oxide phase and subsequently precipitated on the surface to form nanoparticles in doped LST under a high reducing environment.

2.5 Metal doping at B site of LST

The primary drawbacks of LST cathode materials are low ionic conductivity and poor electrocatalytic activity. Doping LST with other metal ions can increase ionic conductivity and improve cell performance. The doping elements on the B-site, such as chromium (Cr), manganese (Mn), and cobalt (Co), which impact the structural stability of perovskite, are mentioned below.

2.5.1 Cr-doped LST

The effect of Cr^{3+} doped on LST was investigated by Du et al. [41]. The cubic structure $La_{0.3}Sr_{0.7}Ti_{1-x}Cr_xO_{3.8}$ (LSTCr) are produced via a solid-state reaction followed by calcination in 5% H_2/Ar at 1300 °C for 10 h. The doping content is 0, 0.1, and 0.2 mol% of Cr^{3+} . It is reported that partial substitution of Ti^{3+} by Cr^{3+} of LSTCr materials decrease the lattice parameter while increase sinter ability. The electrical conductivity of all samples increases with temperature at first, reach a peak, and then drop as the temperature is increased further as show in Fig. 2.6. Total electrical conductivity drop from 230 Scm^{-1} for $x= 0$ to 53 Scm^{-1} for $x= 0.2$ as Cr^{3+} doping

content increases at 800°C. To explore the redox stability of LSTCr, the conductivity is measured in different atmospheres (air and 5% H₂/Ar at 800°C). Fig. 2.7 depicts the conductivity variations of LSTCr with and without Cr doping ($x = 0.2$ and 0) in different atmospheres over time. The overall electrical conductivity is stable and recoverable in various atmospheres, demonstrating remarkable redox stability with Cr doping. According to cell tests, Cr doping improve the electrode performance of LSTCr.

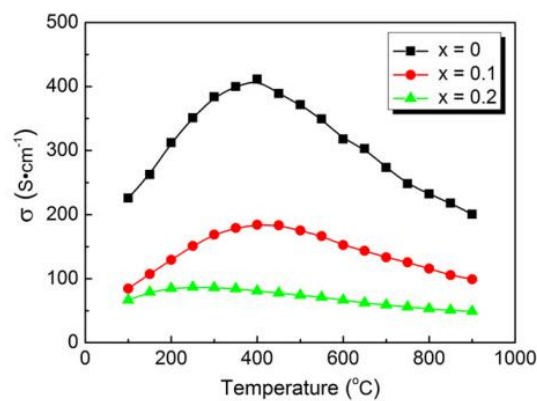


Figure 2.6 Temperature dependence of electrical conductivity of $\text{La}_{0.3}\text{Sr}_{0.7}\text{Ti}_{1-x}\text{Cr}_x\text{O}_{3.δ}$ ($x = 0, 0.1, 0.2$) [41].

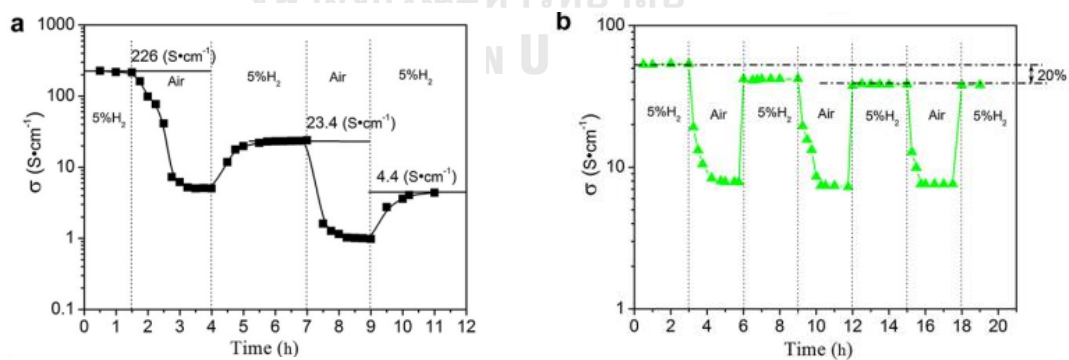


Figure 2.7 Electrical conductivity of $\text{La}_{0.3}\text{Sr}_{0.7}\text{Ti}_{1-x}\text{Cr}_x\text{O}_{3.δ}$ samples at 800°C in alternative atmospheres (air and 5% H₂/Ar) (a) $x = 0$ and (b) $x = 0.2$ [41].

2.5.2 Mn-doped LST

The effect of Mn^{3+} doped on LST was investigated by Rath et al. [42]. The rhombohedral structure $\text{La}_{0.6}\text{Sr}_{0.4}\text{Ti}_{1-x}\text{Mn}_x\text{O}_{3-\delta}$ (LSTM) are produced via a modified sol-gel combustion method using sucrose and pectin as the fuel and catalyst for combustion, respectively. The doping content is 0.2, 0.4, 0.6 and 0.8 mol% of Mn^{3+} . It is reported that the Mn^{3+} substitution at the B-site of the perovskites is a significant impact on the performance of $\text{La}_{0.6}\text{Sr}_{0.4}\text{Ti}_{1-x}\text{Mn}_x\text{O}_{3-\delta}$, with increasing Mn^{3+} content, the electrical conductivity of $\text{La}_{0.6}\text{Sr}_{0.4}\text{Ti}_{1-x}\text{Mn}_x\text{O}_{3-\delta}$ increases in humidified H_2 (97% H_2 + 3% H_2O) as shown in Fig. 2.8. The higher H_2 and CH_4 oxidation rate are caused by an increase in electrical conductivity as well as oxygen vacancy concentration in a reducing atmosphere. Fig. 2.9 shown the maximal power densities of the single cell with the $\text{La}_{0.6}\text{Sr}_{0.4}\text{Ti}_{0.2}\text{Mn}_{0.8}\text{O}_{3-\delta}$ in humidified H_2 and CH_4 at 800°C , are 0.29 Wcm^{-2} and 0.24 Wcm^{-2} , respectively.

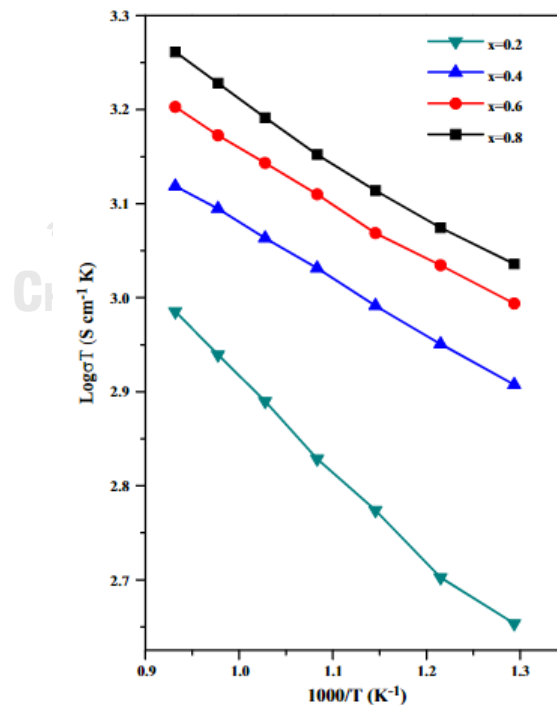


Figure 2.8 Variation of electrical conductivities of $\text{La}_{0.6}\text{Sr}_{0.4}\text{Ti}_{1-x}\text{Mn}_x\text{O}_{3-\delta}$ in humidified H_2 (97% H_2 + 3% H_2O) [42].

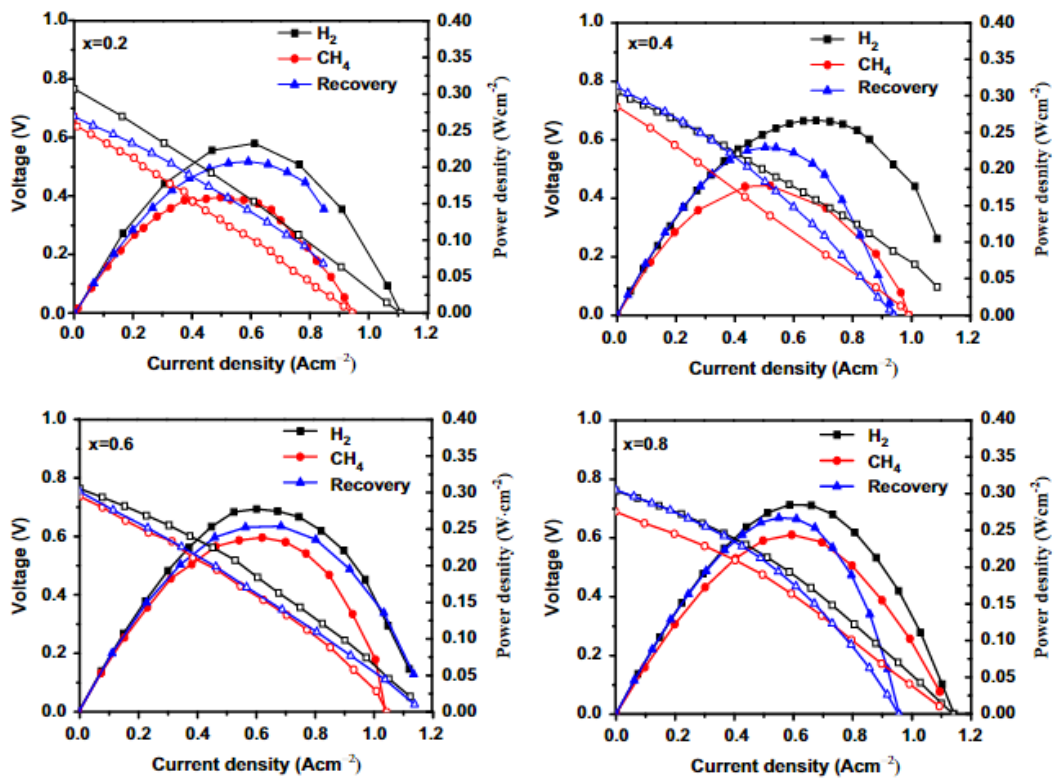


Figure 2.9 Comparison of the I-V curves and power densities of the $\text{La}_{0.6}\text{Sr}_{0.4}\text{Ti}_{1-x}\text{Mn}_x\text{O}_{3.8}$ at 800°C [42].

2.5.3 Co-doped LST

On the oxidation-reduction process, transition metal catalytic activities are often arranged in the following order: $\text{Co} > \text{Mn} > \text{Ni} > \text{Fe} > \text{Cr}$ [43]. Therefore, the effect of Co^{2+} doped on LST was investigated by Cui et al. [44]. The cubic structure $\text{La}_{0.3}\text{Sr}_{0.7}\text{TiO}_{3.8}$ (LST) and $\text{La}_{0.3}\text{Sr}_{0.7}\text{Ti}_{0.93}\text{Co}_{0.07}\text{O}_{3.8}$ (LSTC) are produced via a solid-state reaction, achieving excellent phase purity and refined particle size. Doping Co^{2+} with H_2S -containing H_2 improves catalytic activity and electrochemical performance significantly. Pure H_2 and 5000 ppm H_2S - H_2 are used to test the cells at 800, 850, and 900°C, respectively. The maximum power densities of both electrode catalysts achieved in different feeds and at different temperatures are shown in Fig. 2.10. The power density of both LST and LSTC-based cells increases with temperature in pure

H₂. When the feed are adjusted to 5000 ppm H₂S–H₂, a significant increase in power density are found for both cells. The addition of H₂S improve cell performance by increasing electrode activity. The maximum power density of the LSCT-based cell is around 300 mW·cm⁻² in 5000 ppm H₂S–H₂ at 900 C. Furthermore, all of the results show that LSCT perform much better than LST under the same test conditions.

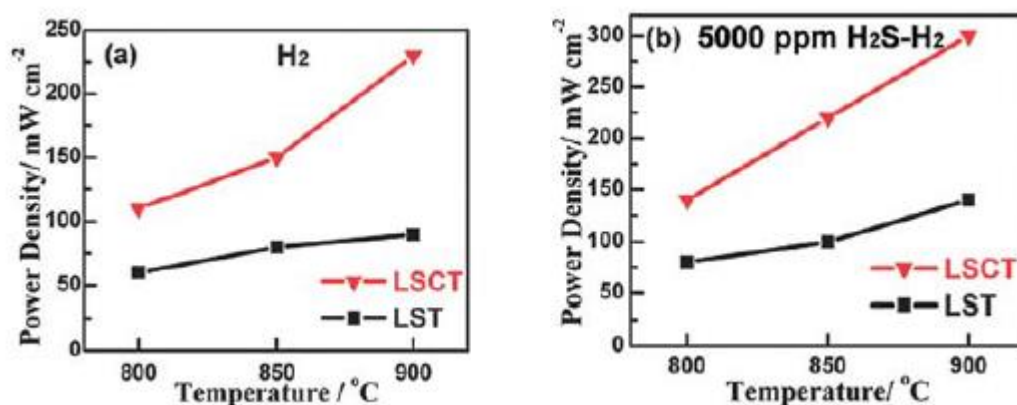


Figure 2.10 Maximum power density of the cells with different fuels: (a) pure H₂ and (b) 5000 ppm H₂S–H₂ at different temperatures [44].

The electrochemical stability test are carried out for 48 h at 900°C using the LSCT-based cell in humid 5000 ppm H₂S–H₂ at a fixed current density of 400 mA·cm⁻² as shown Fig. 2.11. There is no noticeable degradation over the long time period, indicating that the LSCT is electrochemically stable under these environments. This confirmed that the LSCT anode catalyst is not sensitive to the issues that come via the use of Ni cermet in H₂S-containing fuels and that LSCT anode is acceptable sulfur tolerance in SOFCs employing H₂S-containing fuels. The high H₂S content of the feed (5000 ppm) did not poison the catalyst, and no sulfur was deposited on the anode. Moreover, LSCT demonstrate good redox stability, which is crucial to the electrode's durability in practical applications as shown in Fig. 2.12.

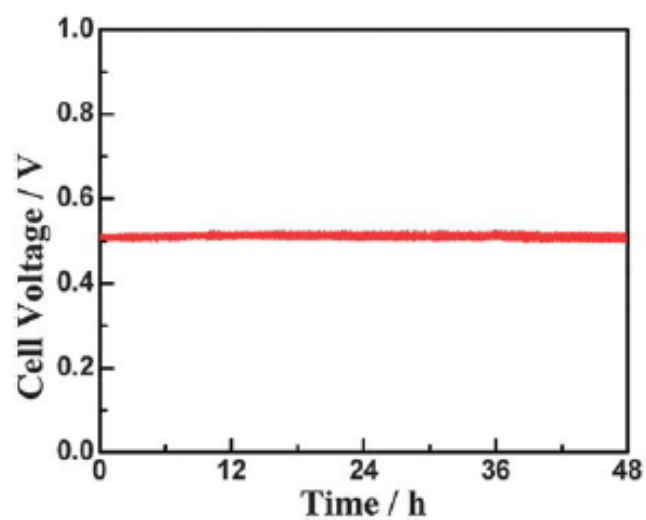


Figure 2.11 Long-term stability test of the LSCT-based cell at $400 \text{ mA}\cdot\text{cm}^{-2}$ and 900°C in humid 5000 ppm H_2S - H_2 feed [44].

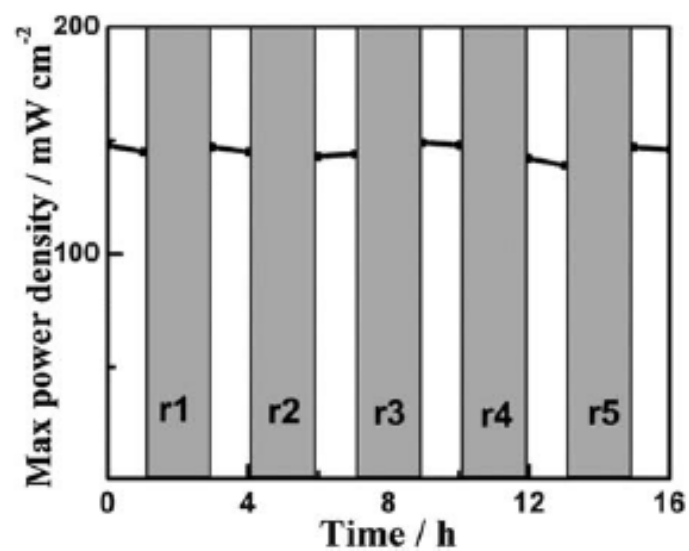


Figure 2.12 Maximum power density of the LSCT-based cell as a function of time at 850°C with H_2 fuel after each redox cycle [44].

2.6 Perovskite synthesis

2.6.1 Solid-state reaction

The solid-state reaction is the simplest method for producing perovskite oxide. The raw materials are nitrates, carbonates, oxides, and other compounds of the A-site and B-site metal ions, which correspond to the perovskite formula ABO_3 , in the needed proportion to obtain the desired composition. Perovskites can be created in solid-state processes mixed by a ball mill then high-temperature calcination to complete the reaction. However, this process added contaminants from raw materials and led to different phases, which influenced perovskite performance. This approach also has limitations due to particle size and a wide range of particle dispersion in the final powder [45].

2.6.2 Co-precipitation

For the preparation of simple oxides, the precipitation of metal salts is a common technique. Precipitation happens following the addition of a chemical reagent that decreases the solubility limit. When distinct cations in a solution precipitate at the same time, this is referred to as co-precipitation. Temperature, concentration, pH, and solution homogeneity must all be controlled for simultaneous precipitation of all cations and perfectly homogenous products. Some of the most often used precipitation reagents are ammonia, ammonium oxalate, urea, and ammonium carbonate. Despite this, due to the sluggish precipitation, the creation of co-precipitated powder takes a long period [45].

2.6.3 Citrate/nitrate combustion method

A thermally induced redox reaction occurs between the oxidant and the fuel. This approach produced a homogeneous, highly reactive, and nano-sized powder. When compared to other traditional methods, a single-phase perovskite powder may

be made at lower calcination temperatures and in shorter time. Citrate/nitrate combustion is one of the most common solution combustion processes, in which citric acid is utilized as the fuel, and metal nitrates are used as the source of metal and oxidant. It is based on the gelling of an organic fuel and the combustion of an aqueous solution containing metal salts, resulting in a fluffy product with a large surface area [46]. Furthermore, nitrates are not removed in the form of NO_x in citrate/nitrate combustion, but rather remain in the mixture with the metal-citrate complex, facilitating auto-combustion. This method has several advantages, including high purity, slight segregation, and accurate monitoring of the perovskite composition [45].



CHAPTER III

EXPERIMENTAL

The experimental methods, which include perovskite cathode powder synthesis, electrolyte preparation and anode preparation, solid oxide electrolysis cell fabrication, and material characterization, are as follows:

3.1 Chemicals and equipment

3.1.1 Chemicals

3.1.1.1 Strontium nitrate, $\text{Sr}(\text{NO}_3)_2$ (>99.0%, Sigma Aldrich)

3.1.1.2 Lanthanum (III) oxide, La_2O_3 ($\geq 99.9\%$, Sigma Aldrich)

3.1.1.3 Cobalt (II) nitrate hexahydrate, $\text{Co}(\text{NO}_3)_2 \cdot 6\text{H}_2\text{O}$ (98%, Sigma Aldrich)

3.1.1.4 Titanium (IV) butoxide, $\text{C}_{16}\text{H}_{36}\text{O}_4\text{Ti}$ (97%, Sigma Aldrich)

3.1.1.5 Citric acid monohydrate, $\text{C}_6\text{H}_8\text{O}_7 \cdot \text{H}_2\text{O}$ (99.5%, Merck)

3.1.1.6 Nitric acid, HNO_3 (65%, Merck)

3.1.1.7 Ammonia, $\text{NH}_3\text{H}_2\text{O}$ (25%, Merck)

3.1.1.8 Lanthanum strontium gallium magnesium, LSGM8282 (Kceracell, Korea)

3.1.1.9 α -terpineol (Fuelcellmaterials, USA)

3.1.1.10 Hydrogen (High purity, TIG, Thailand)

3.1.1.11 Nitrogen (High purity, TIG, Thailand)

3.1.1.12 Carbon dioxide (High purity, TIG, Thailand)

3.1.1.13 100 ppm Hydrogen sulfide in carbon dioxide (High purity, TIG, Thailand)

3.1.1.14 Distilled water

3.1.1.15 Silver ink (Fuelcellmaterials, USA)

3.1.1.16 Platinum mesh and wire (Kceracell, Republic of Korea)

3.1.1.17 Gas sealant (Ultra-Temp 552, Aramco, USA)

3.1.2 Tool and equipment

3.1.2.1 Spoon

3.1.2.2 Beaker

3.1.2.3 Magnetic stirrer

3.1.2.4 Weighing paper

3.1.2.5 Hydraulic pressing pressure 30 tons

3.1.2.6 Mold

3.1.2.7 Hot plate

3.1.2.8 Cylinder

3.1.2.9 Stainless Steel Lab Spatula

3.1.2.11 Two-row mills (SLheater, max mill speed = 500 rpm)

3.1.2.12 Oven

3.1.2.13 Furnace

3.1.2.14 Vatical Furnace (Chavachote, Thailand)

3.1.2.15 HPLC liquid pump (Teledyne SSI, USA)

3.1.2.16 Potentialstat (PG310 Metrohm Autolab, Netherlands)

3.1.2.17 X-Ray Diffractometer, XRD (BRUKER D8 advance)

3.1.2.18 X-ray photoelectron spectroscopy, XPS (AMICUS)

3.1.2.19 Brunauer-Emmett-Teller, BET (ASAP2020, Micromeritics)

3.1.2.20 Scanning electron microscope, SEM (JEOL model S-3400)

3.1.2.21 Thermogravimetric analyses, TGA (TA Instruments SDT Q600)

3.2 Synthesis of perovskite cathode powder by citrate/nitrate combustion method

The compositions of Co-doped LST is presented in Table 3.1. Different amounts of Co^{2+} 0-20%moles were doped into LST structure by substituting the Ti B site.

Table 3.1 The compositions of cathode

Cathode	Doping	Replacing	Abbreviation
$\text{La}_{0.3}\text{Sr}_{0.7}\text{TiO}_{3-\delta}$	-	-	LST
$\text{La}_{0.3}\text{Sr}_{0.7}\text{Ti}_{0.95}\text{Co}_{0.05}\text{O}_{3-\delta}$	0.05 mole of Ti in B site	Ti	$\text{LSTC}_{0.05}$
$\text{La}_{0.3}\text{Sr}_{0.7}\text{Ti}_{0.9}\text{Co}_{0.1}\text{O}_{3-\delta}$	0.1 mole of Ti in B site	Ti	$\text{LSTC}_{0.10}$
$\text{La}_{0.3}\text{Sr}_{0.7}\text{Ti}_{0.85}\text{Co}_{0.15}\text{O}_{3-\delta}$	0.15 mole of Ti in B site	Ti	$\text{LSTC}_{0.15}$
$\text{La}_{0.3}\text{Sr}_{0.7}\text{Ti}_{0.8}\text{Co}_{0.2}\text{O}_{3-\delta}$	0.2 mole of Ti in B site	Ti	$\text{LSTC}_{0.20}$

The $\text{La}_{0.3}\text{Sr}_{0.7}\text{Ti}_{1-y}\text{Co}_y\text{O}_{3-\delta}$ (LSTC) perovskite cathode powder was synthesized by the citrate/nitrate combustion method with $y = 0, 5, 10, 15$ and 20% mol. Perovskite material was synthesized by using $\text{Sr}(\text{NO}_3)_2$, La_2O_3 , $\text{Co}(\text{NH}_3)_2 \cdot 6\text{H}_2\text{O}$ and $\text{C}_{16}\text{H}_{36}\text{O}_4\text{Ti}$ as starting stoichiometric materials and $\text{C}_6\text{H}_8\text{O}_7 \cdot \text{H}_2\text{O}$ as a complexant. Firstly, La_2O_3 was annealed at 1000°C for 4 h before use to eliminate any absorbed water or CO_2 . Then, $\text{C}_{16}\text{H}_{36}\text{O}_4\text{Ti}$ was dissolved in ethanol at a molar ratio of 1:30, followed by the addition of a citric acid solution with a pH of 5 to produce a transparent solution, which was then heated and stirred at 80°C for 1 h. The La_2O_3 , $\text{Co}(\text{NH}_3)_2 \cdot 6\text{H}_2\text{O}$, and $\text{Sr}(\text{NO}_3)_2$ were dissolved in dilute nitric acid solution to generate metal ion solution, the pH of the mixture was adjusted to 5 by 25vol% ammonia solution. After then, the two

solutions were thoroughly mixed together. Citric acid was added to the total amount of metal ions in a 2:1 molar ratio. The final solution was heated and stirred at 80°C until a gel formed. The gel was transferred to an oven and heated at 250°C for 30 min to auto-combustion. Then the fluffy precursor was obtained, which was ground and then calcined at 800°C for 6 h with an interval at 400°C for 2 h to produce LSTC powders. The condition of calcination for LSTC powders are shown in Fig. 3.1.

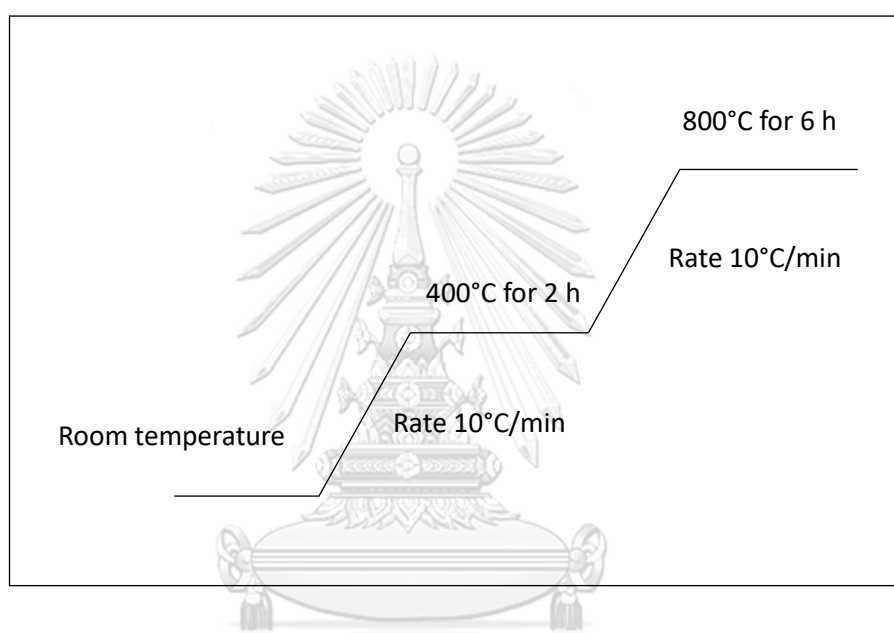


Figure 3.1 The conditions of calcination for LSTC perovskite anode

The performance of different cathode including LST and LSTC were investigated. The LST and LSTC powders were combined with alpha terpineol as a binder to form the cathode ink. Alpha terpineol and cathode powders have a weight ratio of 1:1.

3.3 Electrolyte-supported solid oxide electrolysis cell fabrication

The electrolyte-supported SOECs having different electrode materials were fabricated with LSGM as electrolyte. All the electrolyte-supported cells were

fabricated by doctor blade technique, that investigated the electrolyte-supported cell. The electrolyte-supported cell with the configuration of LST/LSGM/Ag or LSTC/LSGM/Ag were used in this investigated. Three grams of LSGM powders were pressed into a pellet with diameter of 2.54 cm under of 1.7 MPa for 30 seconds, followed by sintering at 1450°C for 10 h. The LST or LSTC ink from 3.2) was applied on one side of LSGM electrolyte with the circular area of 0.5 cm², followed by sintered at 1200°C for 2 h for LST and LSTC. The silver ink was applied on another side of LSGM electrolyte with same circular area, followed by sintered at 900°C for 30 min. The schematic drawing of the electrolyte-supported cell as shown in Fig. 3.2. The electrical connections were made with platinum wires and paste on both electrodes. Finally, the cell was installed in the reactor.

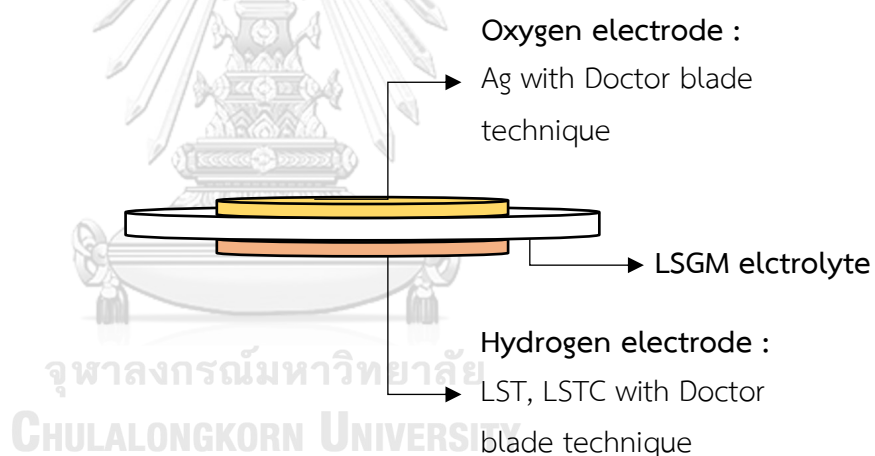


Figure 3.2 Schematic drawing of the electrolyte-supported cell

3.4 Characterization of cathode perovskite

X-ray diffraction (XRD) with a Cu-target X-ray tube (40kV, 30mA) and angles of 2θ range from 20-90° with scan step 0.02° was used to analyze the crystal structure of perovskite oxides. The perovskite was characterized using XRD after it had been calcined. X-ray photoelectron spectroscopy (XPS) was used to study the valence

state of metal and oxygen ion in fine powder. This device determines the chemical valence state, binding energy, and intensity of the photoelectron peak by measuring the energy of photoelectron emission from the surface sample. Brunauer-Emmett-Teller (BET) measured the specific surface area of produced particles. The adsorption of gas molecules on a solid surface is the subject of the BET theory. The total surface area of the particle related to the quantity of adsorbed gas. After the calcination stage, the produced powder was characterized in this experiment. Scanning electron microscope (SEM) was used to study the morphology of fine powder and SOECs. This apparatus generates a picture with remarkable three-dimensional qualities using X-rays or electrons scattered back from the surface illuminated by a restored electron beam. Thermogravimetric analysis (TGA) was used to measure the temperature of powder specimens from room temperature to 1,000°C at a rate of 20°C/min. The perovskite oxides were crushed into fine powder for this experiment, which was carried out in both an air and a N₂ environment.

3.5 Electrochemical performance measurements

Electrochemical performance tests for electrolyte-supported cell was studied at zero current. At $i_{ac}=0$, electrochemical impedance spectroscopy (EIS) measurements were carried out on electrolyte-supported cell with a sinusoidal signal amplitude of 20 mV_{rms} over a frequency range of 0.1MHz to 0.1Hz and a temperature range of 600 to 800°C in air. The EIS data were acquired using a potentiostat/galvanostat equipped with an equivalent circuit as shown in Fig. 3.3.

The I/V curve was obtained using linear sweep current methods. The voltage was controlled between 0.6 and 1.8 V using a potentiostat/galvanostat in galvanostatic mode and a scan rate of 0.1V/s. H₂O, H₂, CO₂, H₂S, and balance gas N₂ were allowed to be fed to the hydrogen electrode in varied compositions. The total flue gas flowrate into the hydrogen electrode was approximately 300 mL/min. Table

3.2 and Fig. 3.4 demonstrate the operating conditions and experimental setup, respectively.

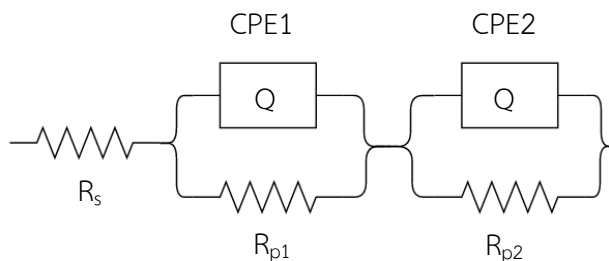


Figure 3.3 Equivalent circuit for impedance response fitting [47]

Table 3.2 Flow rate of each flue gas component for SOEC electrolysis

Name	Composition	Flow rate /mL min ⁻¹				
		H ₂ O	H ₂	CO ₂	CO ₂ +H ₂ S	N ₂
C1	H ₂ O					
	50%	150	20	0	0	130
C2						
	67%	200	20	0	0	80
C3	H ₂ O+CO ₂					
	67%+10%	200	20	30	0	50
C4						
	67%+17%	200	20	50	0	30
C5	H ₂ S					
	10 ppm	200	20	30	30	20
C6						
	15 ppm	200	20	30	45	5

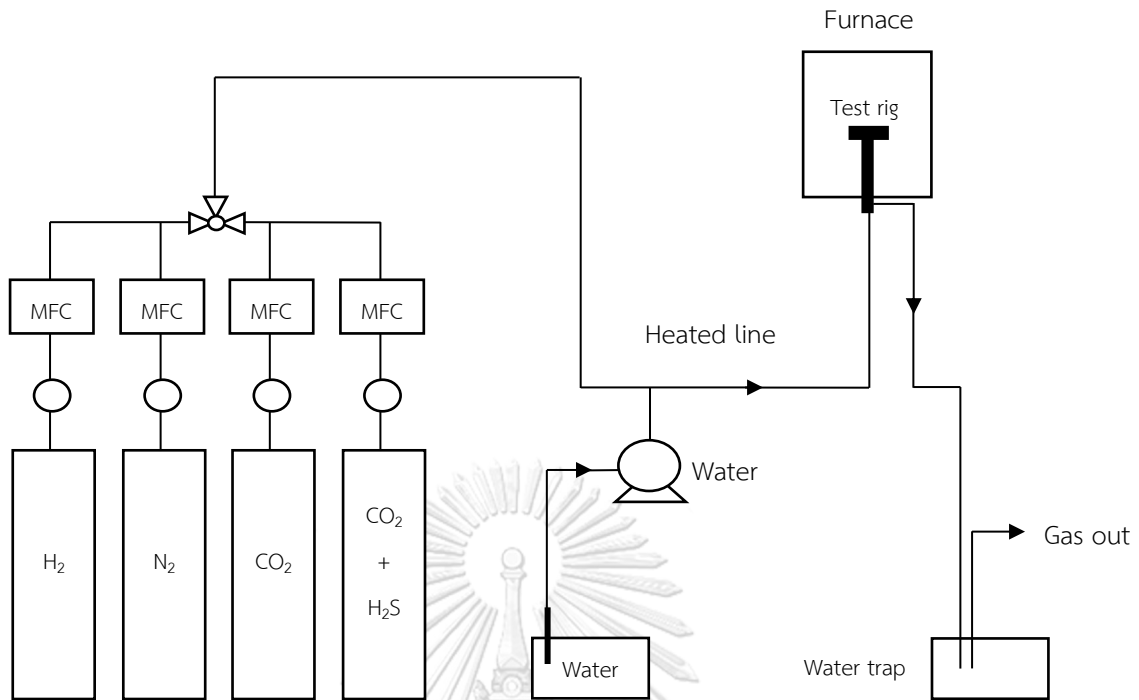


Figure 3.4 Schematic drawing of the test system

The open circuit voltages (OCV) can be calculated by Nernst equation [48, 49] expressed by Eqs. 25 and 26.

$$E_{H_2} = \frac{-\Delta G^\circ(T)_{H_2}}{2F} + \frac{RT}{2F} \ln \frac{y_{H_2} y_{O_2}^{\frac{1}{2}}}{y_{H_2O}} \quad (24)$$

$$E_{CO} = \frac{-\Delta G^\circ(T)_{CO}}{2F} + \frac{RT}{2F} \ln \frac{y_{CO} y_{O_2}^{\frac{1}{2}}}{y_{CO_2}} \quad (25)$$

when E_{H_2} and E_{CO} is the cell potential at the interested temperature of H_2 and CO respectively, $\Delta G^\circ(T)_{H_2}$ and $\Delta G^\circ(T)_{CO}$ is a standard Gibbs free energy of H_2 and CO respectively, R is the universal gas constant ($8.314 \text{ J K}^{-1} \text{ mol}^{-1}$), T is the temperature in kelvins, F is Faraday's constant ($96,485 \text{ C mol}^{-1}$), y_{H_2} , y_{H_2O} , y_{CO} and y_{CO_2} is the mole fraction of H_2 , H_2O , CO , CO_2 and y_{O_2} is the mole fraction of oxygen gas, a constant of 0.21.

CHAPTER IV

RESULTS AND DISCUSSION

The effect of cobalt content in the B-site was investigated in lanthanum, strontium, and titanium doped cobalt ($\text{La}_{0.3}\text{Sr}_{0.7}\text{Ti}_{1-y}\text{Co}_y\text{O}_{3-\delta}$, LSTC) cathodes for solid oxide electrolysis cells. Electrolyte-supported cells (LSTC/LSGM/Ag) were fabricated to determine the electrochemical performance toward $\text{CO}_2/\text{H}_2\text{O}$ electrolysis and sulfur tolerance at intermediate temperature.

4.1 Structural characterizations

X-ray diffraction (XRD) patterns of synthesis $\text{La}_{0.3}\text{Sr}_{0.7}\text{Ti}_{1-y}\text{Co}_y\text{O}_{3-\delta}$ where y is 0, 0.05, 0.1, 0.15 and 0.2 are shown in Fig. 4.1. The main peaks corresponded well to the conventional perovskite structure of SrTiO_3 (JCPDS no. 35-0734). LSTC might be generated via citrate/nitrate combustion, as shown by the diffraction structure of cubic perovskite structure ($\text{Pm}\bar{3}\text{m}$), corresponding to peaks at (100), (110), (111), (200), (210), (211), (220), (300) and (310). According to Fig. 4.1, distinct impurity phases may be found in the diffraction pattern of $\text{La}_{0.3}\text{Sr}_{0.7}\text{Ti}_{1-y}\text{Co}_y\text{O}_{3-\delta}$ where y is 0, 0.05, 0.15 and 0.2, perhaps as a result of formation of La_2O_3 (JCPDS no. 54-0213) or $\text{La}(\text{OH})_3$ (JCPDS no. 36-1481). The existence of impurity phases may be due to a co-precipitation of metal oxide phase or an incomplete solid state reaction during calcination [50]. Increased Co^{2+} -doping caused the peak locations (110) at $2\theta = 32.4$ to shift to a higher diffraction angle due to a reduced lattice parameter, as shown in the magnified scale in Fig. 4.1(b). Lattice parameters and lattice volumes calculated using Bragg's Law were shown in Table 4.1. The difference lattice parameter was due to the different in size between cobalt and titanium cations, taking into consideration the ionic radius of Co^{4+} (0.053 nm), Co^{3+} (LS: 0.0545 nm, HS: 0.061 nm), Co^{2+} (0.0745 nm), Ti^{4+} (0.0605 nm), Ti^{3+} (0.0670) [51]. Because cobalt is more vulnerable to

oxidation state modification than titanium, the charge compensation mechanism is projected to shift from 'A-site vacancy production' to 'B-site transition metal oxidation state change' when the cobalt concentration increases [52]. Therefore, increased Co^{2+} -doping at the B-site on LST may be compatible with the decrease in lattice parameter and unit cell volume. The crystallite sizes of the catalyst samples were calculated using the Scherrer's equation. The average crystallite size of LST, $\text{LSTC}_{0.05}$, $\text{LSTC}_{0.10}$, $\text{LSTC}_{0.15}$, and $\text{LSTC}_{0.20}$ were 22.99, 30.03, 28.82, 24.53, and 21.33 nm, respectively. It appears that crystallite size increased with an increase in cobalt doping in LST due to cobalt incorporation then decreased from 30.03 to 21.33 nm when the cobalt concentration was increased from 5 to 20 %mol. According to the results of the XRD results, perovskite crystals were formed in all of the samples. The peak location was shifted towards larger angles by the doping method, which had an impact on the structure of LST in that an increased doping concentration resulted in a decreased crystallite size [50, 53].

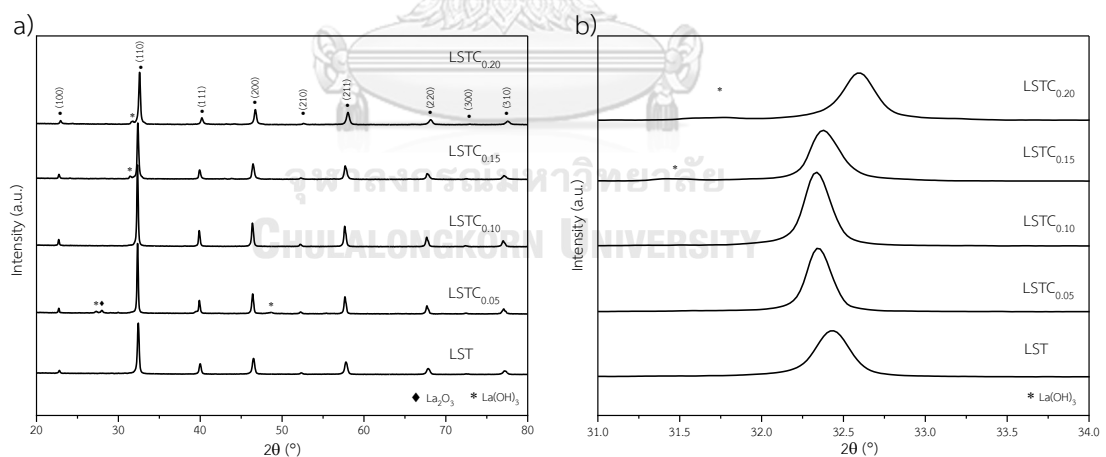


Figure 4.1 XRD patterns of $\text{La}_{0.3}\text{Sr}_{0.7}\text{Ti}_{1-y}\text{Co}_y\text{O}_{3-\delta}$ (LSTC) where $y = 0, 0.05, 0.1, 0.15$ and 0.2 : **a)** after sintered in air at 1200°C for 2 h; and **b)** magnified scale at 2θ angles between 31° and 34°

Table 4.1 The lattice parameters and lattice volumes of $\text{La}_{0.3}\text{Sr}_{0.7}\text{Ti}_{1-y}\text{Co}_y\text{O}_{3-\delta}$ (LSTC)

Cathode	Lattice parameter (Å)	Lattice volume (Å ³)
LST	3.9010	59.3664
LSTC _{0.05}	3.9106	59.8029
LSTC _{0.10}	3.9117	59.8556
LSTC _{0.15}	3.9060	59.5926
LSTC _{0.20}	3.8823	58.5143

After being sintered at 1200°C for 2 h, the SEM images and the EDX mapping of the LSTC perovskite powder were shown in Fig. 4.2 and 4.3, respectively. A homogeneous morphology with high porosity and the creation of larger sample agglomerates were observed. The LSTC powder had an irregular form and a diameter less than 2 μm . The LSTC particle size was comparatively larger than the LST, which corresponding to the XRD patterns which showed narrower main-peak patterns. According to Fig 4.3, EDX element mapping revealed a homogenous distribution of La, Sr, Ti, and Co in the samples to confirm the composition of the obtained sample. Additionally, the element composition on the surface of each sample was shown in Table 4.2, and the corresponding specific surface areas for LST, LSTC_{0.05}, LSTC_{0.10}, LSTC_{0.15}, and LSTC_{0.20} were 7.0516, 5.8658, 7.2709, 4.6496 and 7.4935 m^2/g , respectively. The creation of the La_2O_3 and $\text{La}(\text{OH})_3$ phases can be related to the decrease in specific surface area.

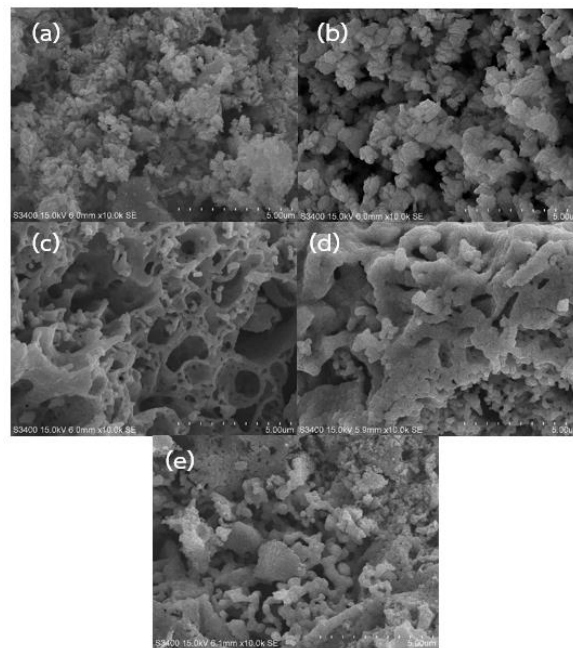


Figure 4.2 SEM images of $\text{La}_{0.3}\text{Sr}_{0.7}\text{Ti}_{1-y}\text{Co}_y\text{O}_{3-\delta}$ (LSTC) sintered at 1200°C for 2 h:

(a) LST, (b) $\text{LSTC}_{0.05}$, (c) $\text{LSTC}_{0.10}$, (d) $\text{LSTC}_{0.15}$, and (e) $\text{LSTC}_{0.20}$

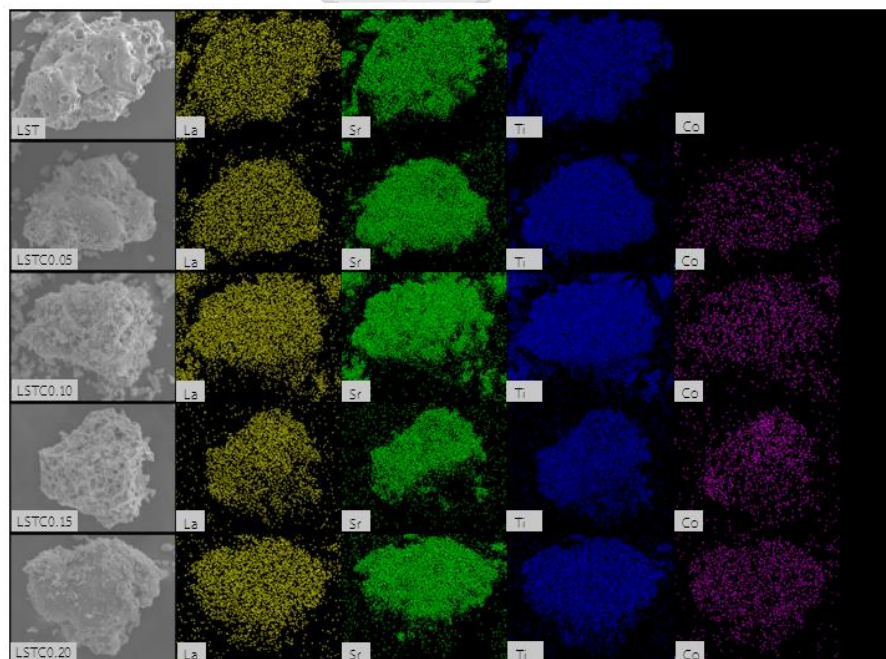


Figure 4.3 EDX images of $\text{La}_{0.3}\text{Sr}_{0.7}\text{Ti}_{1-y}\text{Co}_y\text{O}_{3-\delta}$ (LSTC) find powder where $y = 0, 0.05,$

0.1, 0.15 and 0.2 which sintered at 1200°C for 2 h.

Table 4.2 The stoichiometry of $\text{La}_{0.3}\text{Sr}_{0.7}\text{Ti}_{1-y}\text{Co}_y\text{O}_{3-\delta}$ where $y = 0, 0.05, 0.1, 0.15$ and 0.2 which sintered at 1200°C for 2 h calculated from EDX analysis.

Cathode	EDX results			
	La	Sr	Ti	Co
$\text{La}_{0.3}\text{Sr}_{0.7}\text{TiO}_{3-\delta}$	0.288	0.712	1	-
$\text{La}_{0.3}\text{Sr}_{0.7}\text{Ti}_{0.95}\text{Co}_{0.05}\text{O}_{3-\delta}$	0.338	0.662	0.898	0.102
$\text{La}_{0.3}\text{Sr}_{0.7}\text{Ti}_{0.9}\text{Co}_{0.1}\text{O}_{3-\delta}$	0.320	0.680	0.893	0.107
$\text{La}_{0.3}\text{Sr}_{0.7}\text{Ti}_{0.85}\text{Co}_{0.15}\text{O}_{3-\delta}$	0.309	0.691	0.801	0.199
$\text{La}_{0.3}\text{Sr}_{0.7}\text{Ti}_{0.8}\text{Co}_{0.2}\text{O}_{3-\delta}$	0.303	0.697	0.720	0.280

4.2 Thermogravimetric analysis

The thermal stability of LST and LSTC was measured using TGA on the sample powders from room temperature (RT) to 800°C in air. Metal ion oxidation and thermal reduction were related to the loss of weight. As seen in Fig. 4.4, the weight loss behavior in the TGA profiles under air atmosphere, it was observed that the mass of the samples continued to decrease as temperature increased. The weight loss results from the release of oxygen, which led to an increase in concentration of oxygen vacancies in the LSTC sample. Due to the evacuation of absorbed water, the initial weight loss was seen at approximately 270°C . Then, it has been noted that LSTC has continued weight loss as the temperature increased. This weight loss profile could be related to more oxygen vacancies produced in LSTC [54, 55]. As shown in Fig. 4.4, the weight loss in air for LST, $\text{LSTC}_{0.05}$, $\text{LSTC}_{0.10}$, $\text{LSTC}_{0.15}$ and $\text{LSTC}_{0.20}$ were 0.87%, 1.56%, 0.13%, 0.49% and 0.94%, respectively. Co-doped sample shows a high temperature compared to that without Co-doping, demonstrating that Co-doping can enhance the structural stability of $\text{La}_{0.3}\text{Sr}_{0.7}\text{Ti}_{1-y}\text{Co}_y\text{O}_{3-\delta}$ [56].

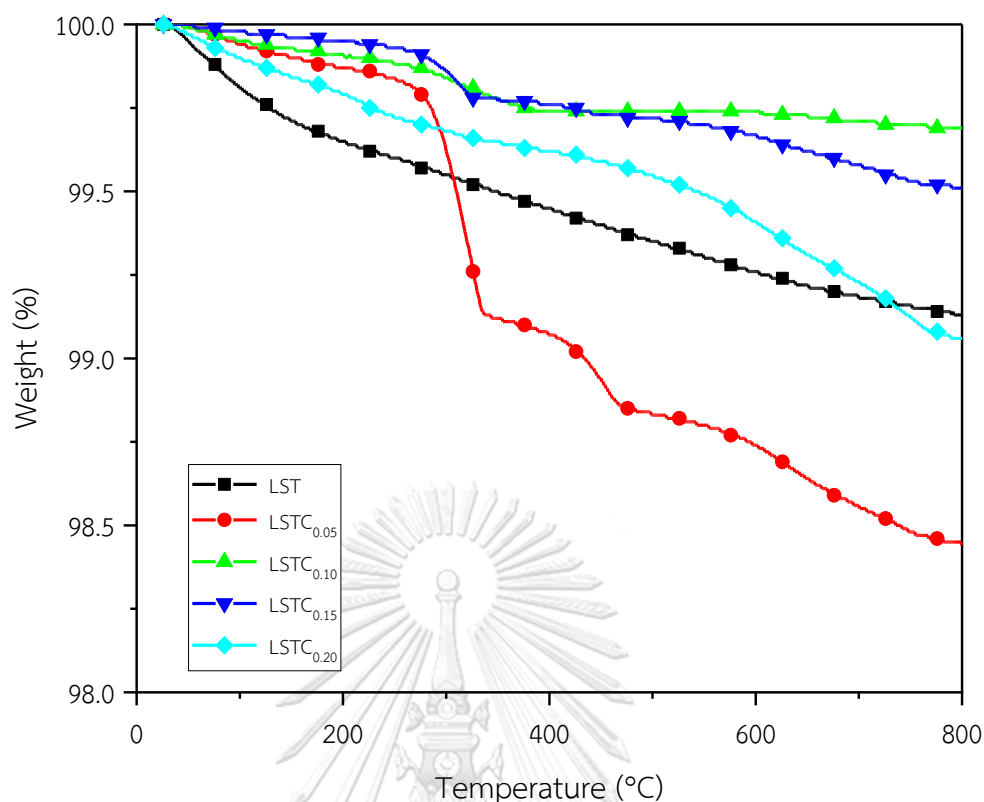


Figure 4.4 TGA profile of $\text{La}_{0.3}\text{Sr}_{0.7}\text{Ti}_{1-y}\text{Co}_y\text{O}_{3.8}$ (LSTC) find powder where $y = 0, 0.05, 0.1, 0.15$ and 0.2 which sintered at 1200°C for 2 h in air at room temperature to 800°C

4.3 X-ray photoelectron spectroscopy analysis

After sintering at 1200°C for 2 hours, the cobalt valance states of LSTC perovskite powder were determined by XPS analysis. The $\text{La}3d$, $\text{Sr}3d$, $\text{Ti}2p$, $\text{Co}2p$, $\text{O}1s$, and $\text{C}1s$ were seen on the XPS survey spectra, as shown in Fig. 4.5.

The $\text{O} 1s$ region of the XPS spectra was deconvoluted into three peaks, shown in Fig. 4.6(a). The peaks centered around at 529.3, 531.6, and 533.4 eV. The first peak at 529.3 eV appears to be related to the metal ions at sites A and B and represents lattice oxygen species. The second oxygen peak, which is about 2.3 eV higher than the metal oxygen peak at 531.6 eV, represents surface-adsorbed hydroxyl

species. Approximately 4.1 eV higher than the metal oxygen peak, the third oxygen peak is observed to have binding energy of 533.4 eV. A surface-adsorbed carbonate species is thought to be related to this peak [50, 57-60]. Oxygen species can be divided into the lattice oxygen (O_{lattice}) and adsorbed oxygen (O_{adsorbed}) [57, 61]. The area under the XPS peaks can be used to determine the oxygen vacancies on the perovskite lattice, which are typically related to the ratio of O_{adsorbed} to O_{lattice} [62]. In this study, the ratio of $O_{\text{adsorbed}}/O_{\text{lattice}}$ increased when LST was doped with cobalt, then decreased with increased cobalt content, as shown in Table 4.3. As a result, Co-doping may have influenced the concentration of oxygen vacancies as well as the pathway for oxygen ion transport [56]. The oxygen vacancies on the surface of perovskite oxides could serve as sites for CO_2 activation and adsorption during the electrochemical reduction of CO_2 [63].

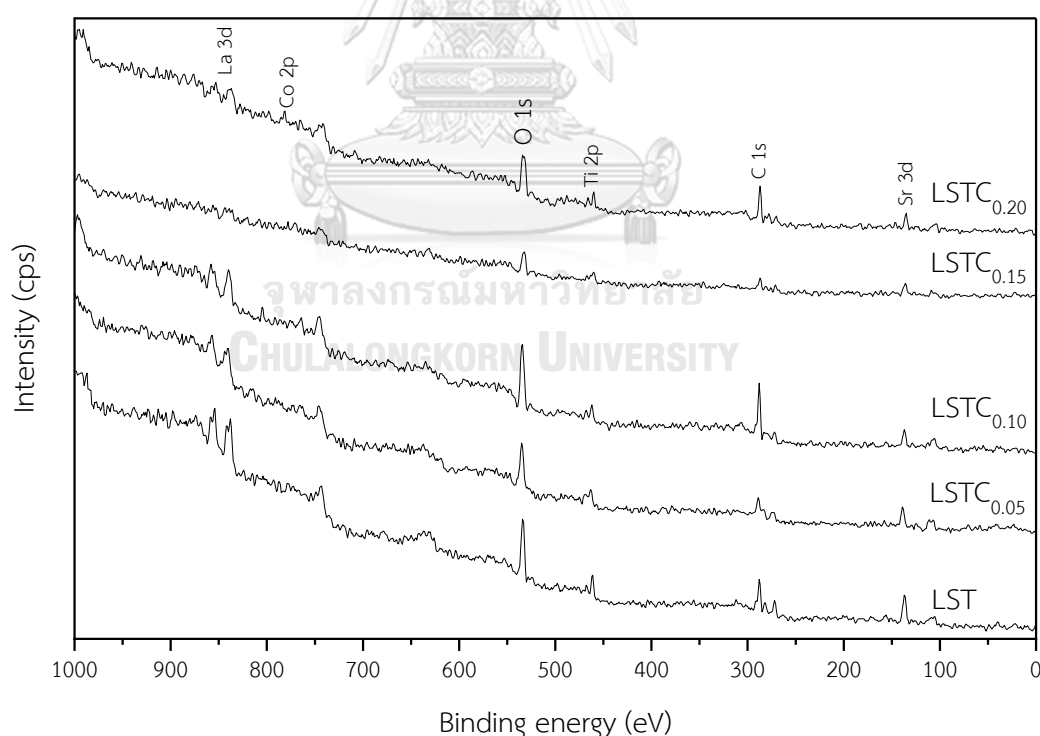


Figure 4.5 Low resolution XPS spectra of $\text{La}_{0.3}\text{Sr}_{0.7}\text{Ti}_{1-y}\text{Co}_y\text{O}_{3-\delta}$ (LSTC) ($0 \leq y \leq 0.2$) powder

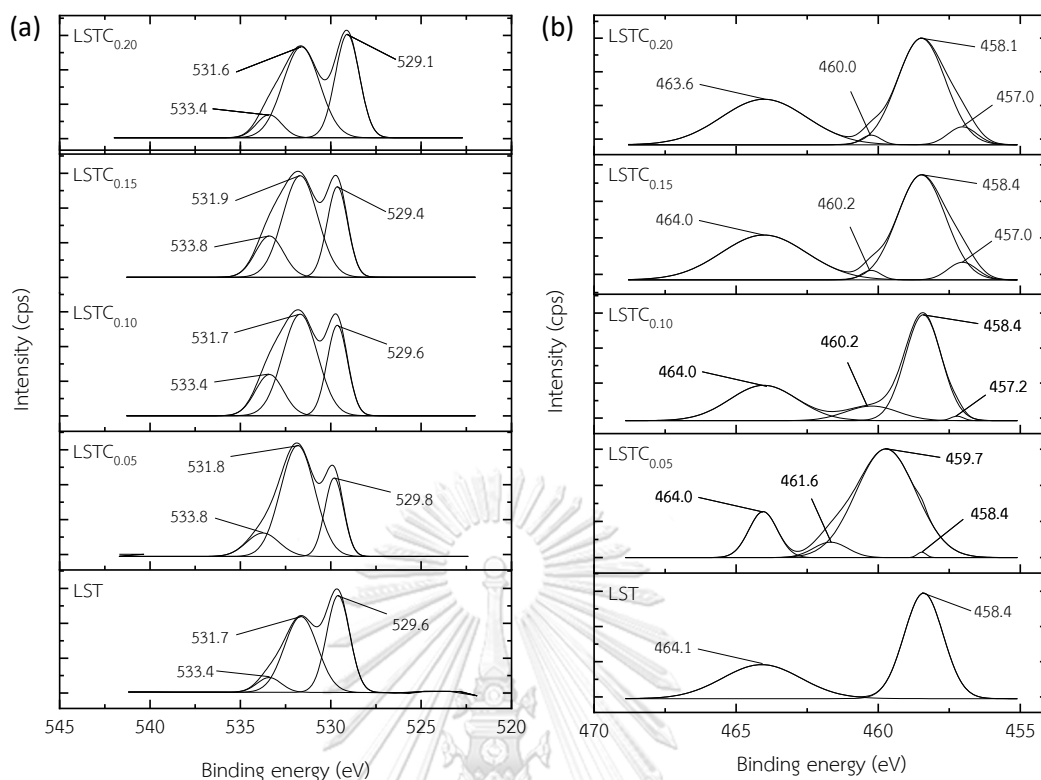


Figure 4.6 The deconvoluted of XPS spectra of $\text{La}_{0.3}\text{Sr}_{0.7}\text{Ti}_{1-y}\text{Co}_y\text{O}_{3-\delta}$ (LSTC) ($0 \leq y \leq 0.2$) powder: (a) O 1s, and (b) Ti 2p

Table 4.3 The $\text{O}_{\text{adsorbed}}/\text{O}_{\text{lattice}}$ ratio for various cobalt contents.

y value in $\text{La}_{0.3}\text{Sr}_{0.7}\text{Ti}_{1-y}\text{Co}_y\text{O}_{3-\delta}$	%Area		$\text{O}_{\text{adsorbed}}/\text{O}_{\text{lattice}}$
	$\text{O}_{\text{adsorbed}}$	$\text{O}_{\text{lattice}}$	
0	56.13	43.87	1.28
0.05	75.53	24.47	3.08
0.10	71.69	28.31	2.53
0.15	59.82	40.82	1.45
0.20	61.07	38.93	1.57

For deconvolution of the Ti 2p XPS spectra, LST presented binding energies of 458.4, and 464.1, which was assigned to $\text{Ti}^{4+} 2p_{3/2}$ and $\text{Ti}^{4+} 2p_{1/2}$, respectively. In comparison of LSTC, two additional Ti 2p peaks from the LST were found at 457 eV and 460 eV, which can be related to the existence of Ti^{3+} . This study showed that in Co-doped samples, Ti^{4+} was partly converted to Ti^{3+} [42, 50, 57-60, 64, 65]. Table 4.4, contains the calculated $\text{Ti}^{3+}/\text{Ti}^{4+}$ ratio based on peak regions. It can be seen that increasing Co^{2+} doping at the B-site to LSTC increased $\text{Ti}^{3+}/\text{Ti}^{4+}$ ratio. This suggested that Ti^{4+} was mostly reduced to Ti^{3+} during the charge compensation process in $\text{La}_{0.3}\text{Sr}_{0.7}\text{Ti}_{1-y}\text{Co}_y\text{O}_{3-\delta}$ [42]. Some oxygen vacancies can be formed in the crystal lattice when the valence state of the Ti ion decreases. As a result of charge compensation, the electron concentration can rise, significantly enhancing the electrical conductivity [64].

Co 2p intensities and area under the XPS spectra were nearly invisible, as shown in Fig. 4.5. However, the Co 2p XPS region may be divided into two main peaks ($\text{Co } 2p_{3/2}$ and $\text{Co } 2p_{1/2}$). According to Fig. 4.7, the peaks in $\text{Co } 2p_{3/2}$ at 779 and $\text{Co } 2p_{1/2}$ at 795 eV [44, 66]. It is rather difficult to evaluate the area under Co 2p XPS spectra due to the low Co concentration in $\text{La}_{0.3}\text{Sr}_{0.7}\text{Ti}_{1-y}\text{Co}_y\text{O}_{3-\delta}$.

Table 4.4 The $\text{Ti}^{3+}/\text{Ti}^{4+}$ ratio for various cobalt contents.

y value in $\text{La}_{0.3}\text{Sr}_{0.7}\text{Ti}_{1-y}\text{Co}_y\text{O}_{3-\delta}$	%Area		$\text{Ti}^{3+}/\text{Ti}^{4+}$
	Ti^{3+}	Ti^{4+}	
0	0	100	0.00
0.05	6.88	93.12	0.07
0.10	11.64	88.36	0.13
0.15	7.25	92.75	0.08
0.20	19.30	80.70	0.24

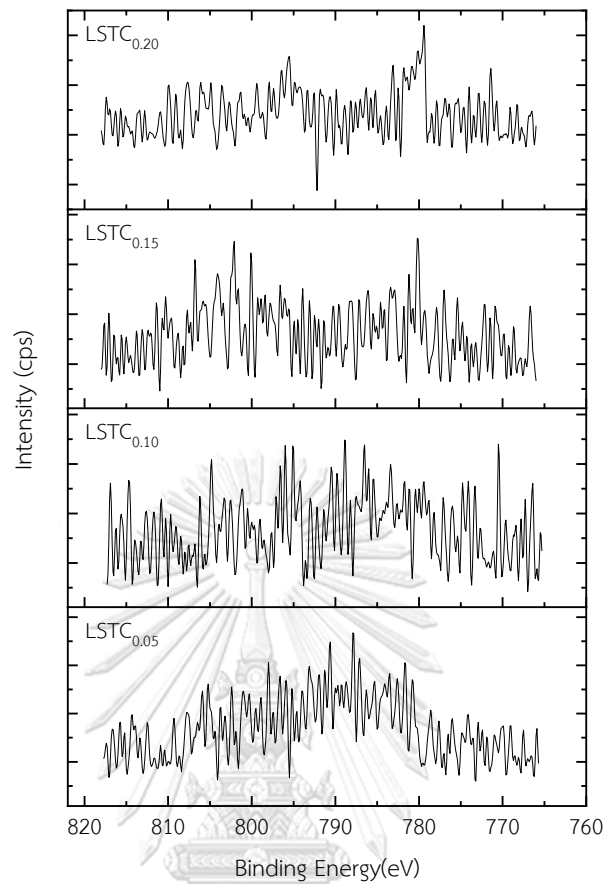


Figure 4.7 The deconvoluted of Co 2p XPS spectra of $\text{La}_{0.3}\text{Sr}_{0.7}\text{Ti}_{1-y}\text{Co}_y\text{O}_{3-\delta}$ (LSTC) ($0 \leq y \leq 0.2$) powder

4.4 Calculation of tolerance factor (t)

The tolerance factor (t) of $\text{La}_{0.3}\text{Sr}_{0.7}\text{Ti}_{1-y}\text{Co}_y\text{O}_{3-\delta}$ were calculated from Eqs. 22, where r_A , r_B , and r_O are the ionic radius of A-site, B-site and oxygen ion, respectively. It should be noted that r_A and r_B are the sum of the ionic radii (r_{La} , r_{Sr} for r_A and r_{Ti} , r_{Co} for r_B) in the ABO_3 perovskite structure multiplied by corresponding amounts. The orthorhombic and hexagonal phases will form when $0.75 < t < 0.9$ and $t > 1.04$, respectively, whereas the cubic phase can be maintained with $0.95 \leq t \leq 1.04$ [67]. The tolerance factor of LSTC slightly decreased from 0.99 to 0.98 as cobalt doping

content increased from 0 to 0.20, indicating a stable perovskite structure for all compositions [67-69]. The typically allowed range of the measured t-factors indicated that no severely distorted perovskite crystals had formed as a result of the addition of Co.

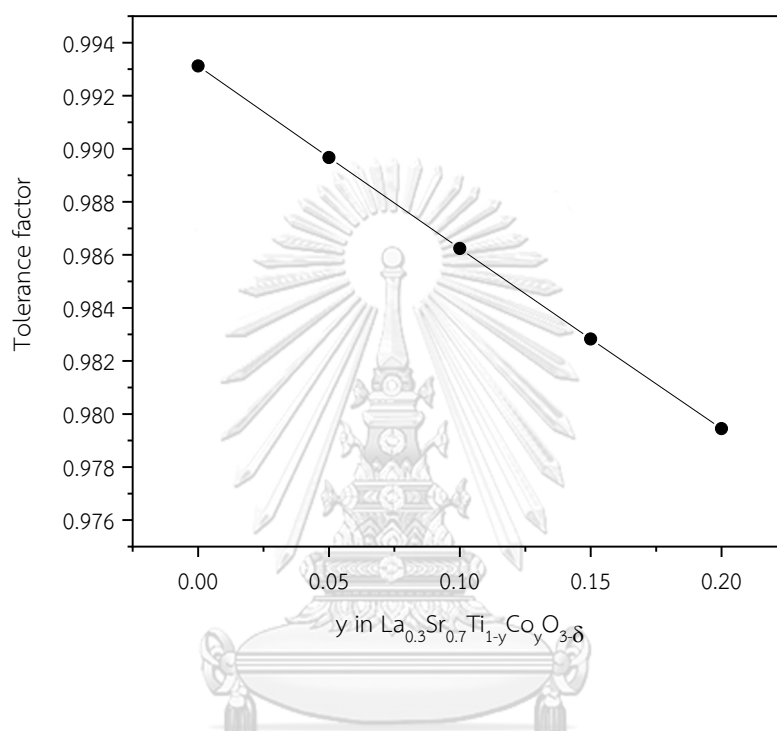


Figure 4.8 Tolerance factor of $\text{La}_{0.3}\text{Sr}_{0.7}\text{Ti}_{1-y}\text{Co}_y\text{O}_{3-\delta}$ (LSTC) ($0 \leq y \leq 0.2$) powder at room temperature

4.5 Electrochemical performance

An electrolyte-supported cell with LSGM as the electrolyte (LSTC/LSGM/Ag) was used for the EIS measurement in ambient air. In general, polarization resistance interpretation for electrolyte-supported cell may be described as two partly resolved arcs: high frequency (HF) and low frequency (LF). The initial intercept of the x-axis of the Nyquist plot provided the ohmic resistance (R_{Ohmic}), which was related to the electrolyte lattice resistance and lead response. The HF arc (R_{HF}) represents the

polarization resistance of charge transfer which was related to the oxygen reduction process, while the LF arc (R_{LF}) represents the polarization resistance of mass transport which was related to the gas phase diffusion [70, 71]. It was reported that hydrogen electrode's gas diffusion is represented by a frequency of 1–10 Hz, the oxygen electrode's oxygen surface exchange and oxygen bulk diffusion are represented by a frequency of 10–200 Hz, and the hydrogen electrode's charge transfer reaction and ionic transport are represented by a frequency of more than 200 Hz [72]. The electrochemical performance of electrolyte supported LSTC/LSGM/Ag of varying Co contents from 0 to 20%mol are shown in Fig. 4.9(a-e), respectively. The steam electrochemical performance of the SOEC was studied in relation to the effects of various operating temperatures while the feed composition was controlled at a constant C1 (50% H_2O , 6.67% H_2). The linear sweep approach was applied to characterize the single polarization while the operating potential was varied from 0.6 to 1.8 V. The LSTC_{0.10}/LSGM/Ag produced the highest current density at varied working temperatures between 600 and 800°C. The current density of the electrolyte supported having a LSTC_{0.10} cathode increased from -0.05 to -1.08 at a constant potential at 1.8 V as the temperature rise from 600°C to 800°C. The open circuit voltage (OCV) drop from 1.03 V to 0.83 V as the temperature rise from 600°C to 800°C, corresponding to calculated potential using the Nernst equation. However, the measure OCV of LSTC_{0.10}/LSGM/Ag in this work was about 0.7 V, which corresponded to the leakage in sealing around the cell. The electrochemical performance of the cell was decreased as the Co content of the cathode increased while they were still much higher than that of LST [73].

Fig. 4.10(a) and 4.10(b) show a comparison of I/V profiles and electrochemical impedance responses at OCV of different Co concentrations ranging from 0 to 20%mol at an operating temperature of 800 °C and the feed composition was controlled at a constant C1 (50% H_2O , 6.67% H_2). At 1.8 V, the highest current densities

of electrolyte-supported LSTC/LSGM/Ag of varying Co contents from 0 to 20%mol were -0.38, -0.15, -1.08, -0.04 and -0.15 A/cm², respectively.

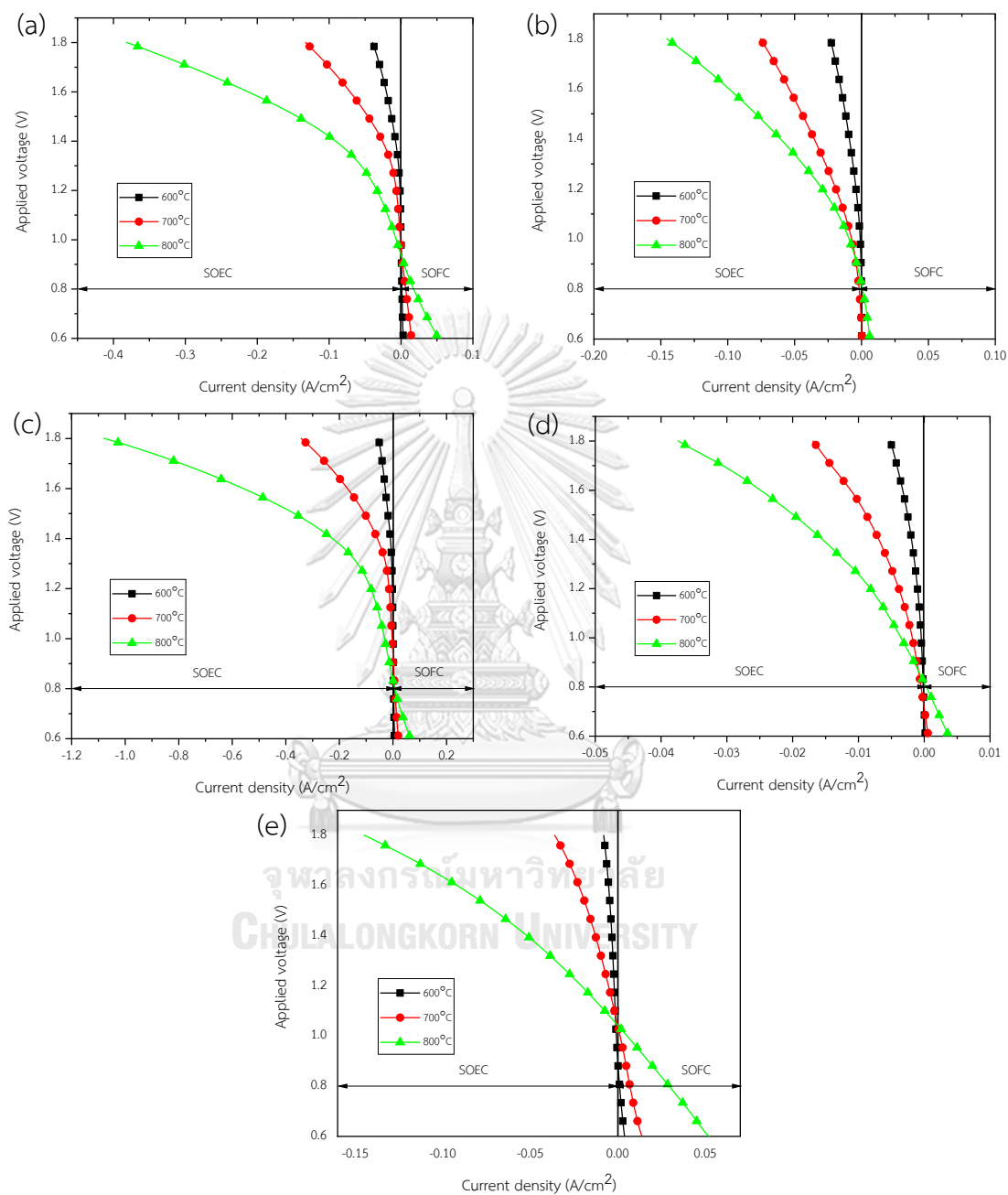


Figure 4.9 Comparison of the electrochemical performance of various operating temperature and C1 (50%H₂O, 6.67%H₂) feed composition: a) LST, b) LSTC_{0.05}, c) LSTC_{0.1}, d) LSTC_{0.15}, and e) LSTC_{0.2}

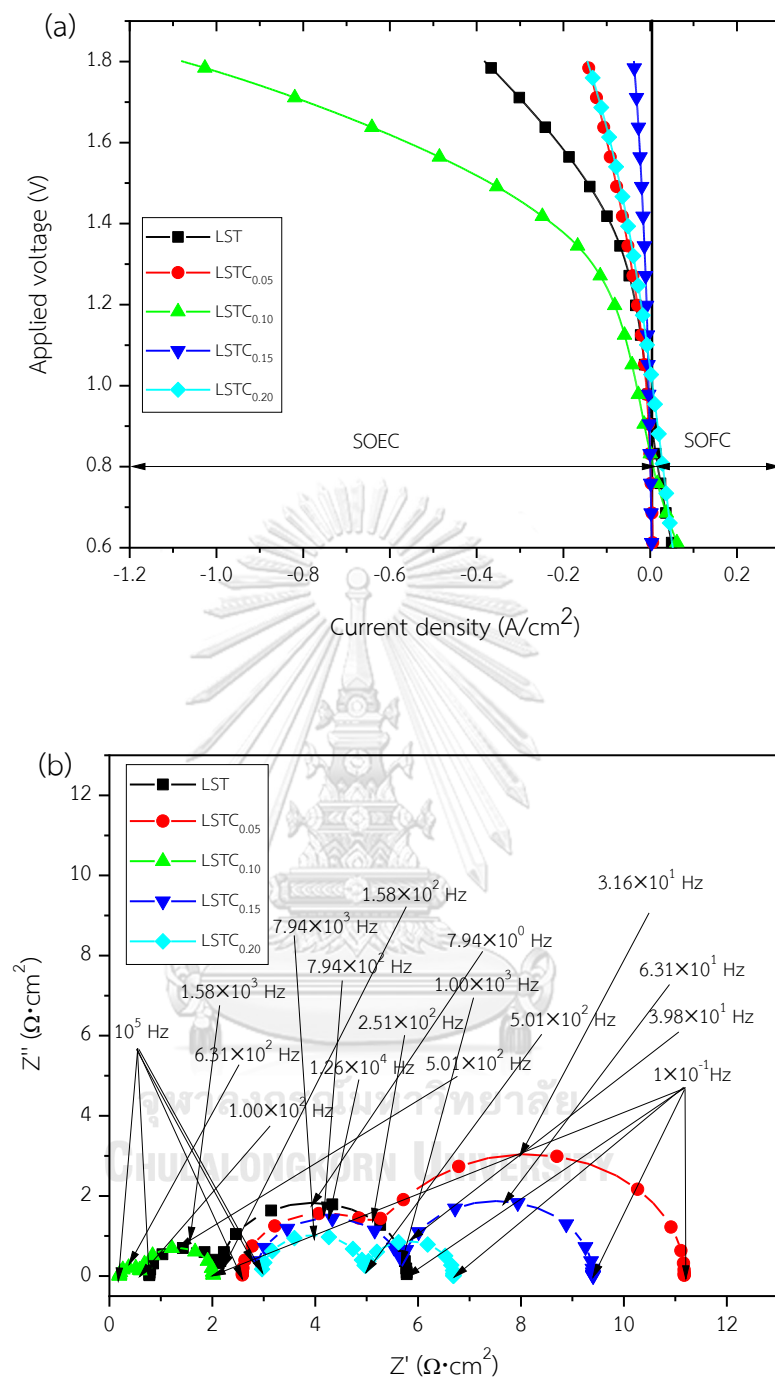


Figure 4.10 Comparison of the electrochemical performance of various Co contents from 0 to 20%mol and the feed composition was controlled at a constant C1 (50% H_2O , 6.67% H_2) at 800°C: (a) IV profiles, and (b) electrochemical impedance response (EIS)

As can be observed in Fig. 4.10(b), the suitable amount of Co loading at 10%mol provided decreased in the polarization resistance (HF and LF area). Table 4.5 shows the Ohmic resistance and polarization in both the HF and LF regions. The addition of Co content should increase the activation resistance while decreasing the mass transport resistance because of the improved porosity [74, 75]. The impedance arc cannot be separated between these two characteristic resistances. For the ohmic resistance increased rapidly with Co content increases, but then decreased rapidly when amount of Co loading at 10%mol. The ohmic loss varies depending on the design and production of the cell. The ohmic resistances of the electrolyte, electrodes and interfaces between the electrodes and the electrolyte, and between the electrodes and current collectors determine ohmic losses, which result from the resistance to charge conduction via the different cell components [76-79]. However, it was observed that LSTC_{0.10} had the lowest total polarization resistance which can be explained by the mixed ionic and electronic conductivity (MIEC) characteristics of the LSTC material and the dopant characteristics at the B-site on the LST. The XPS results showed that LSTC_{0.10} had a high oxygen vacancy, which improved oxygen mobility during oxygen diffusion on the oxygen electrode. For perovskite oxides, the oxygen ionic conduction mainly depends on oxygen vacancy concentrations at a specific temperature and carrier mobility, referring to B-O interactions between metal and lattice oxygen ion and the geometrical component of lattice structure. At high temperatures, Co⁴⁺ tend to decrease more readily to Co³⁺ than Ti⁴⁺, which results in the formation of an appropriate amount of oxygen ion vacancies [73]. The oxygen vacancy concentration will increase with Co-doping while the Ti³⁺ concentration will decrease. The former causes an increase in ionic conductivity, whereas the latter causes an electronic conductivity decrease. The strength of the B-O bond diminishes in the order Ti > Cr > Mn > Cu > Fe > Co. As a result, Co-doping in La_{0.3}Sr_{0.7}Ti_{1-y}Co_yO_{3-δ} can improve oxygen ion mobility. As a result, the hydrogen electrode performance of LSTC_{0.10} was optimized and the total polarization resistance was lowest.

The performance of the Co-electrolysis was studied in relation to the effects of various feed compositions while the temperature was controlled at a constant 800°C. The electrochemical performance of electrolyte supported LSTC/LSGM/Ag of varying Co contents from 0 to 20%mol are shown in Fig. 4.11(a-e), respectively. The LSTC_{0.10}/LSGM/Ag produced the highest current density at varied Co contents from 0 to 20%mol. The current density and OCVs of the electrolyte supported by having a LSTC_{0.10} cathode decreased as CO₂ and H₂S content in feed composition increasing, the OCV would drop from 1.04 V to 0.77 V. The ratio of hydrogen to steam determines the OCV, assuming that there is only a half-reaction (Eqs. 12). The Nernst equation predicts that observed OCV variations are greater than estimated OCV variations. The highest current densities at 1.8 V of electrolyte-supported LSTC_{0.10}/LSGM/Ag with varying feed compositions C1 to C6, the current density decreased slightly: 1.08, -1.02, -1.05, -0.98, -0.92, -0.91 A/cm² for condition C1 to C6 respectively.

Table 4.5 Resistance of the various electrolyte support LSTC/LSGM/Ag of various Co contents from 0 to 20%mol and the feed composition was controlled at a constant C1 (50%H₂O, 6.67%H₂) at 800°C. R_{Ohmic}, R_{HF} and R_{LF} are referred to ohmic resistance and polarization resistance in high frequency region and low frequency region, respectively

cc	Area specific resistance ($\Omega \cdot \text{cm}^2$)			
	R _{Ohmic}	R _{HF}	R _{LF}	R _T
0	0.78	1.34	3.66	5.78
0.05	2.58	2.57	6.02	11.17
0.10	0.19	0.42	1.41	2.02
0.15	2.89	2.79	3.72	9.40
0.20	3.00	1.98	1.71	6.69

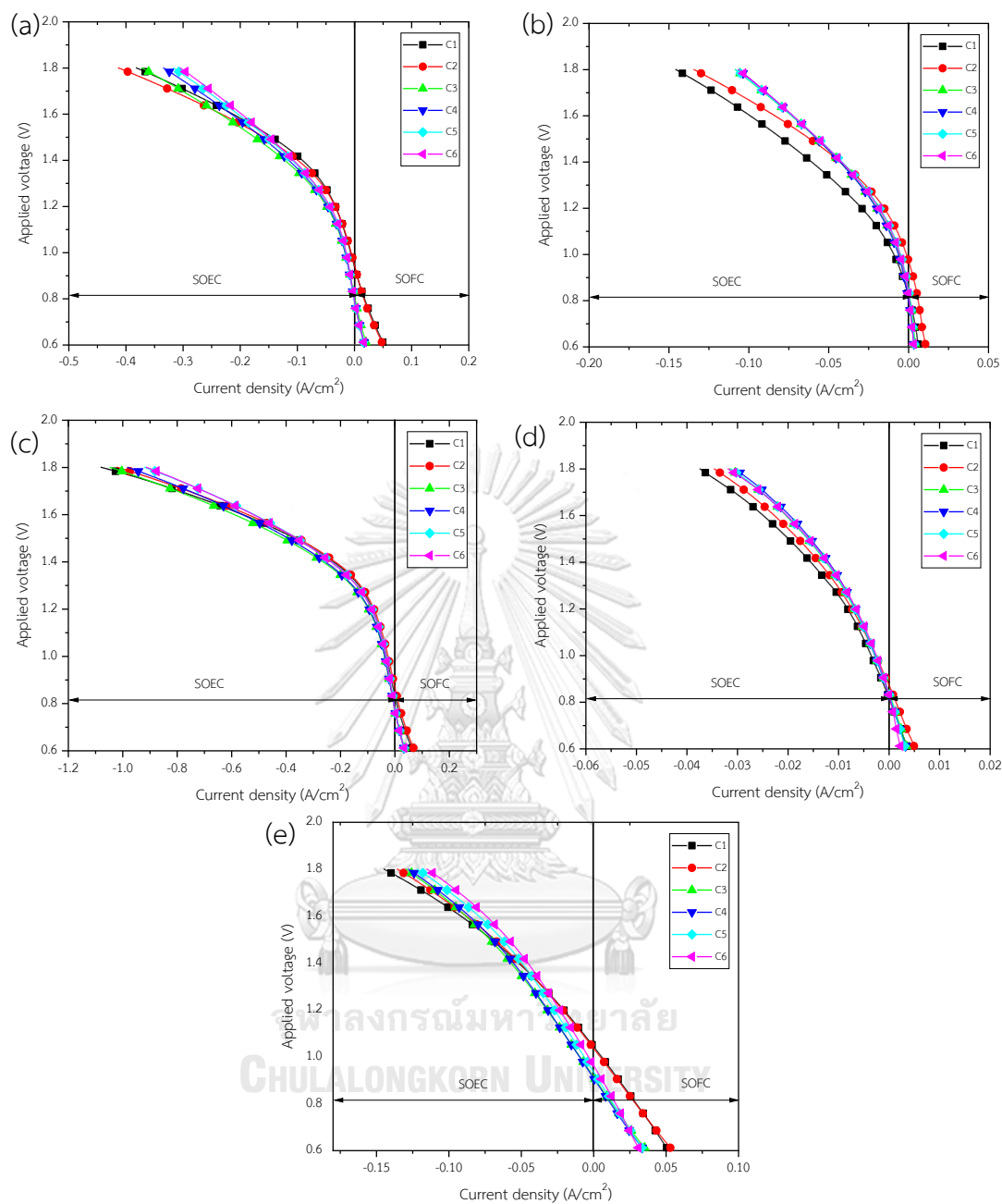


Figure 4.11 Comparison of the electrochemical performance of various feed composition at 800°C: (a-e) electrolyte-supported of $\text{La}_{0.3}\text{Sr}_{0.7}\text{Ti}_{1-y}\text{Co}_y\text{O}_{3.8}$ (LSTC) with varying Co contents from 0 to 20%mol, respectively

Fig. 4.12(a) shows a comparison of IV profiles at 800°C of various Co contents from 0 to 20%mol and the feed composition was controlled at a constant C6 (15 ppm H₂S). At 1.8 V, the highest current densities of electrolyte-supported LSTC_{0.10}/LSGM/Ag showed the greatest performance. Then, the electrochemical impedance response of LSTC_{0.10}/LSGM/Ag with various feed compositions was investigated as shown in Fig. 4.12(b). It is evident that R_{Ohmic} , R_p , and R_T increased when input CO₂ and H₂S feed to system, with R_p changing the most. Table 4.6 shows that the R_T data slightly decreased from 2.91 to 2.01 $\Omega\cdot\text{cm}^{-2}$ as the steam level increased from 50% to 67%. This suggests that a greater steam concentration within this range is advantageous for the enhancement of electrochemical performance [48]. CO₂ and H₂S were added to the system with maintaining the H₂O content at 67%. It can be seen that R_T increased when added CO₂ and H₂S into system. Table 4.6 shows that the R_T data increased from 2.01 to 2.69 $\Omega\cdot\text{cm}^{-2}$ for C2 and C3 feed composition, respectively. When H₂S was added at 10 ppm with 10% CO₂ and H₂O 67%, the R_T data increased from 2.01 to 2.89 $\Omega\cdot\text{cm}^{-2}$ for C2 and C5 feed composition, respectively. It was found that the R_T remained consistent when the concentration of CO₂ and H₂S was increased. It could be due to the slight variation in CO₂ and H₂S contents. The Nyquist plot (Fig. 4.12(b)), the intercept of the impedance arc with the real axis at the high-frequency domain represents the R_{Ohmic} , with contributions mostly from the LSGM electrolyte; whereas the intercept of the impedance arc with the real axis at the low-frequency end represents the R_T , with the difference between these two intercepts representing the R_p . With input of CO₂ and H₂S, the R_{Ohmic} marginally increased. However, R_p increased significantly when CO₂ and H₂S concentration increased. The difference in H₂ and H₂O diffusions may be the cause of the higher polarization losses of the cathode under co-electrolysis conditions, which may be the cause of the higher ASR. The performance of the co-electrolysis process can be dominated by CO₂ and H₂S diffusion resistance, since R_{LF} was clearly the largest component of the impedance and obviously dependent on the increase in

CO_2 and H_2S . Additionally, water gas shift and reverse water gas shift reactions (WGS/RWGS) as well as sulfur chemisorption reaction can also affect the co-electrolysis process, affecting the $\text{LSTC}_{0.10}$ and R_{LF} [44, 48].

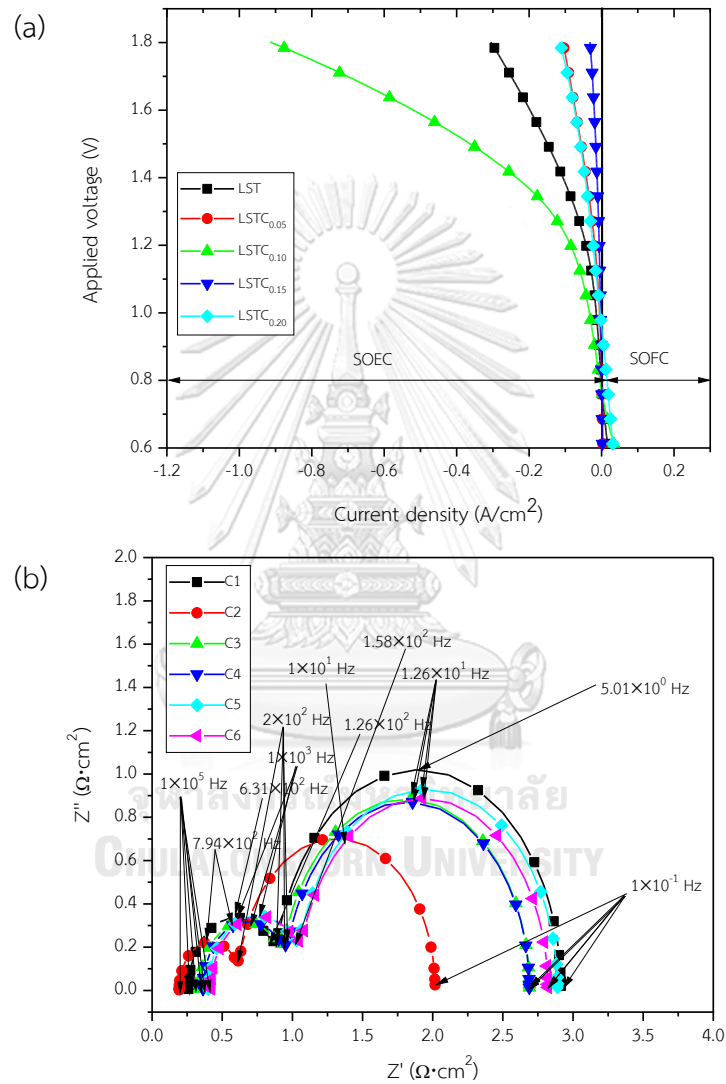


Figure 4.12 Comparison of the electrochemical performance at 800°C: (a) IV profiles, of various Co contents from 0 to 20%mol and the feed composition was controlled at a constant C6 (15 ppm H_2S), and (b) electrochemical impedance response (EIS) of $\text{LSTC}_{0.10}/\text{LSGM}/\text{Ag}$ with various feed compositions

Table 4.6 Resistance of the various feed composition of LSTC_{0.10}/LSGM/Ag at 800°C.

R_{Ohmic} , R_{HF} and R_{LF} are referred to ohmic resistance and polarization resistance in high frequency region and low frequency region R_{T} are total resistance, respectively

Feed compositions	Area specific resistance ($\Omega \cdot \text{cm}^2$)			
	R_{Ohmic}	R_{HF}	R_{LF}	R_{T}
C1	0.25	0.63	2.03	2.91
C2	0.19	0.42	1.40	2.01
C3	0.34	0.59	1.76	2.69
C4	0.36	0.59	1.74	2.69
C5	0.40	0.63	1.86	2.89
C6	0.42	0.64	1.76	2.82

Fig. 4.13, 4.14 and Table 4.7 shows a comparison of performance durability of LST/LSGM/Ag and LSTC_{0.10}/LSGM/Ag. After 24 h of durability test, the ohmic resistance and total polarization resistance of all electrolyte-support cells were increased. For LST/LSGM/Ag, the ohmic resistance increased from 1.50 to 2.95 $\Omega \cdot \text{cm}^2$ and the total polarization resistance increase 41.20% from 6.02 to 8.50 $\Omega \cdot \text{cm}^2$ after 24 hours. And for LSTC_{0.10}/LSGM/Ag, the ohmic resistance increased from 0.42 to 0.61 $\Omega \cdot \text{cm}^2$ and the total polarization resistance increase 37.23% from 2.82 to 3.87 $\Omega \cdot \text{cm}^2$ after 24 hours. These can be offered about through metal agglomeration, which lowers mass transport resistance, and lowers activation resistance. It can be indicated that LST cathode showed the highest increase of total polarization resistance, whereas LSTC_{0.10} cathode showed a lowest increase with operating time.

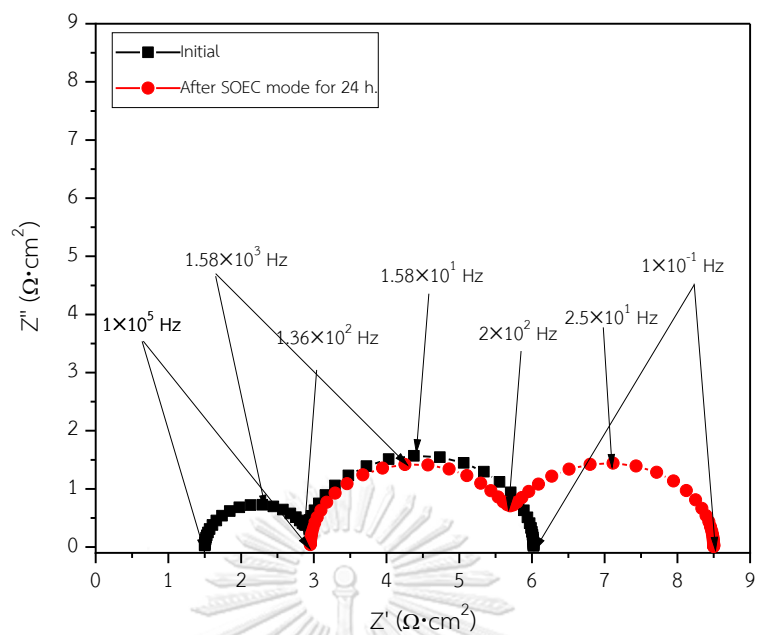


Figure 4.13 Comparison of LST/LSGM/Ag electrochemical impedance response at different duration (800 °C with C6 feed composition for 24 h)

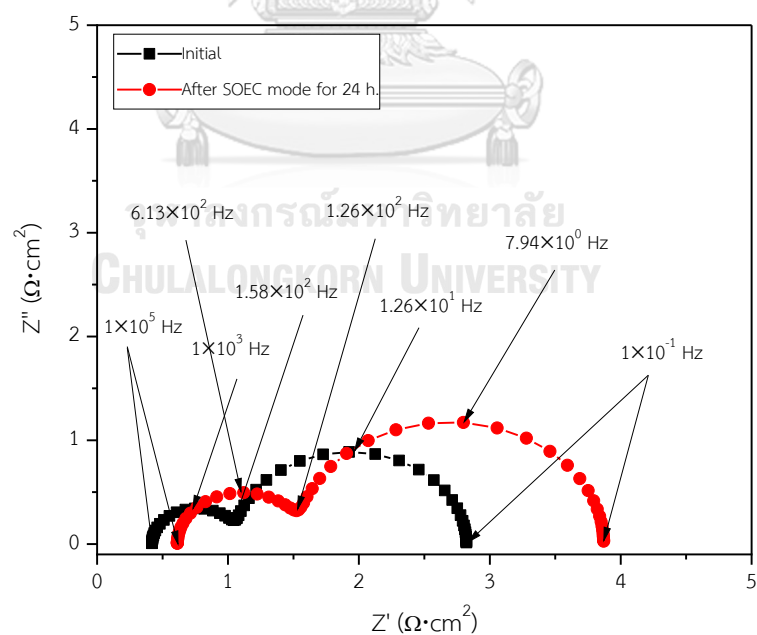


Figure 4.14 Comparison of LSTC_{0.10}/LSGM/Ag electrochemical impedance response at different duration (800 °C with C6 feed composition for 24 h)

Table 4.7 Resistance of LST/LSGM/Ag and LSTC_{0.10}/LSGM/Ag at 800°C with C6 feed composition for 24 h. R_{Ohmic} , R_{HF} and R_{LF} are referred to ohmic resistance and polarization resistance in high frequency region and low frequency region R_{T} are total resistance, respectively

Duration (h)	Area specific resistance ($\Omega \cdot \text{cm}^2$)							
	LST/LSGM/Ag				LSTC _{0.10} /LSGM/Ag			
	R_{Ohmic}	R_{HF}	R_{LF}	R_{T}	R_{Ohmic}	R_{HF}	R_{LF}	R_{T}
0	1.50	1.49	3.03	6.02	0.42	0.64	1.76	2.82
24	2.95	2.75	2.80	8.50	0.61	0.91	2.35	3.87



CHAPTER V

CONCLUSIONS

$\text{La}_{0.3}\text{Sr}_{0.7}\text{Ti}_{1-y}\text{Co}_y\text{O}_{3-\delta}$ ($0 \leq y \leq 0.2$) perovskite cathode powder were successfully synthesized by the citrate/nitrate combustion method. LSTC exhibited single phase perovskite after sintered at 1200°C for 2 h while La_2O_3 and $\text{La}(\text{OH})_3$ were observed in other sample except sample with $y = 0.10$. In TGA analysis, weight loss was attributed to metal ion oxidation and thermal reduction; it was found that as temperature increases, the mass of the samples decreases. The weight loss in air for LST, $\text{LSTC}_{0.05}$, $\text{LSTC}_{0.10}$, $\text{LSTC}_{0.15}$ and $\text{LSTC}_{0.20}$ was 0.87%, 1.56%, 0.13%, 0.49% and 0.94%, respectively. This weight loss profile may be attributed to increased oxygen vacancies formed in LSTC. For XPS spectra, the valence state of O 1s and Ti 2p were characterized. $\text{O}_{\text{adsorbed}}/\text{O}_{\text{lattice}}$ increased when cobalt was doped in LST, then decreased with increased cobalt content. Furthermore, increasing the partial substituting of Co^{2+} doping at the B-site to LSTC increased $\text{Ti}^{3+}/\text{Ti}^{4+}$ ratio, and oxygen vacancies can develop in the crystal lattice when the valence state of the Ti ion decreases, enhancing the electrical conductivity. The tolerance factor value was nearly 1 when increased cobalt content, which mean that doping with Co^{2+} could help maintain the structural stability of LSTC.

The electrolyte-supported cell was then fabricated to test the performance of each $\text{La}_{0.3}\text{Sr}_{0.7}\text{Ti}_{1-y}\text{Co}_y\text{O}_{3-\delta}$. Electrochemical performance of electrolyte-support LSTC/LSGM/Ag was investigated. The cell having cathode with 10%mol loading shows the highest current density at 800 °C compared to the other compositions. The current density was -1.08 A/cm^2 at operating voltage of 1.8 V using 50% H_2O and 6.67% H_2 of the feed composition. The cell performance of $\text{LSTC}_{0.10}$ cathode increased with increasing the operating temperature, while the feed composition of H_2O led to decreased total polarization resistance.

For co-electrolysis and sulfur tolerance, the $\text{LSTC}_{0.10}/\text{LSGM}/\text{Ag}$ produced the highest current density. The highest current densities at 1.8 V of electrolyte-supported $\text{LSTC}_{0.10}/\text{LSGM}/\text{Ag}$ decreased slightly, while R_{ohmic} , R_p , and R_T increased

when added CO_2 and H_2S in the system. It was found that the R_T remained consistent when the concentration of CO_2 and H_2S was increased due to the slight variation in CO_2 and H_2S contents. While the electrochemical performance decreased. For LST/LSGM/Ag, R_T increased from 6.02 to 8.50 $\Omega \cdot \text{cm}^2$ and $\text{LSTC}_{0.10}/\text{LSGM/Ag}$, R_T increased from 2.82 to 3.87 $\Omega \cdot \text{cm}^2$ after 24 hours.



REFERENCES

- [1] Cheng K, Kang J, King DL, Subramanian V, Zhou C, Zhang Q, Wang Y. Advances in Catalysis for Syngas Conversion to Hydrocarbons. *Advances in Catalysis*. 60: Elsevier; 2017. p. 125-208.
- [2] Jensen SH, Larsen PH, Mogensen M. Hydrogen and synthetic fuel production from renewable energy sources. *International Journal of Hydrogen Energy*. 2007;32(15):3253-7.
- [3] Mingyi L, Bo Y, Jingming X, Jing C. Thermodynamic analysis of the efficiency of high-temperature steam electrolysis system for hydrogen production. *Journal of Power Sources*. 2008;177(2):493-9.
- [4] Ni M, Leung M, Leung D. Technological development of hydrogen production by solid oxide electrolyzer cell (SOEC). *International Journal of Hydrogen Energy*. 2008;33(9):2337-54.
- [5] Ye L, Xie K. High-temperature electrocatalysis and key materials in solid oxide electrolysis cells. *Journal of Energy Chemistry*. 2021;54:736-45.
- [6] Sreedhar I, Agarwal B, Goyal P, Singh SA. Recent advances in material and performance aspects of solid oxide fuel cells. *Journal of Electroanalytical Chemistry*. 2019;848.
- [7] กรมพัฒนาพลังงานทดแทนและอนุรักษ์พลังงาน. การนำความร้อนทิ้งกลับมาใหม่. คู่มือประกอบการฝึกอบรมหลักสูตร "ผู้รับผิดชอบด้านพลังงานสามัญ (โรงงาน)". ปทุมธานี: กองพัฒนาทรัพยากรบุคคลด้านพลังงาน; 2553. p. 1-35.
- [8] Koo B, Kim K, Kim JK, Kwon H, Han JW, Jung W. Sr Segregation in Perovskite Oxides: Why It Happens and How It Exists. *Joule*. 2018;2(8):1476-99.
- [9] Zhou X, Yan N, Chuang KT, Luo J. Progress in La-doped SrTiO₃(LST)-based anode materials for solid oxide fuel cells. *RSC Adv*. 2014;4(1):118-31.
- [10] Song C, Liu K, Subramani V. Introduction to Hydrogen and Syngas Production and Purification Technologies. New Jersey: John Wiley & Sons, Inc.; 2009.
- [11] Wang Y, Liu, T., Fang, S., Xiao, G., Wang, H., Chen, F. A novel clean and effective syngas production system based on partial oxidation of methane assisted solid oxide

co-electrolysis process. *Journal of Power Sources*. 2015;277:261–7.

[12] Elder Rachael CD, Mogensen Mogens Bjerg. Carbon Dioxide Utilisation-Closing the Carbon Cycle. *High Temperature Electrolysis*. 2015. p. 183-209.

[13] Udagawa J, Aguiar P, Brandon NP. Hydrogen production through steam electrolysis: Model-based steady state performance of a cathode-supported intermediate temperature solid oxide electrolysis cell. *Journal of Power Sources*. 2007;166(1):127-36.

[14] Hongpeng He XH, Liquan Chen. Sr-doped LaInO_3 and its possible application in a single layer SOFC. *Solid State Ionics*. 2000;130:183–93.

[15] Zhang W, Yu B, Xu J. Investigation of single SOEC with BSCF anode and SDC barrier layer. *International Journal of Hydrogen Energy*. 2012;37(1):837-42.

[16] Liu Y, Meng Y, Zhang W, Wang B, Afzal M, Xia C, Zhu B. Industrial grade rare-earth triple-doped ceria applied for advanced low-temperature electrolyte layer-free fuel cells. *International Journal of Hydrogen Energy*. 2017;42(34):22273-9.

[17] Ruiz-Morales JC, Canales-Vázquez J, Marrero-López D, Pérez-Coll D, Peña-Martínez J, Núñez P. An all-in-one flourite-based symmetrical solid oxide fuel cell. *Journal of Power Sources*. 2008;177(1):154-60.

[18] Kim S-D, Yu J-H, Seo D-W, Han I-S, Woo S-K. Hydrogen production performance of 3-cell flat-tubular solid oxide electrolysis stack. *International Journal of Hydrogen Energy*. 2012;37(1):78-83.

[19] S.P. J. Sintering behavior of $\text{Ni/Y}_2\text{O}_3\text{-ZrO}_2$ cermet electrodes of solid oxide fuel cells. *Journal of Materials Science*. 2003;38(18):3775 - 82.

[20] Goodenough JB, Huang Y-H. Alternative anode materials for solid oxide fuel cells. *Journal of Power Sources*. 2007;173(1):1-10.

[21] Sun C, Stimming U. Recent anode advances in solid oxide fuel cells. *Journal of Power Sources*. 2007;171(2):247-60.

[22] Marcin B, Janusz J, Agata Z. Determination of H_2S and HCl concentration limits in the fuel for anode supported SOFC operation. *Open Chemistry*. 2013;11(6):960-7.

[23] Sasaki K, Haga K, Yoshizumi T, Minematsu D, Yuki E, Liu R, Uryu C, Oshima T, Ogura T, Shiratori Y, Ito K, Koyama M, Yokomoto K. Chemical durability of Solid Oxide Fuel Cells: Influence of impurities on long-term performance. *Journal of Power Sources*.

2011;196(22):9130-40.

[24] Shu L, Sunarso J, Hashim SS, Mao J, Zhou W, Liang F. Advanced perovskite anodes for solid oxide fuel cells: A review. *International Journal of Hydrogen Energy*. 2019;44(59):31275-304.

[25] Patel NK, Utter RG, Das D, Pecht M. Surface degradation of strontium-based perovskite electrodes of solid oxide fuel cells. *Journal of Power Sources*. 2019;438:227040-7.

[26] Miruszewski T, Gdaniec P, Rosinski W, Karczewski J, Bochentyn B, Kusz B. Structure and electrical properties of Y, Fe-based perovskite mixed conducting composites fabricated by a modified polymer precursor method. *Solid State Sciences*. 2017;70:41-6.

[27] Zhao J. First-principles study of ferroelectricity in oxide superlattices. French: South China Normal University; 2013.

[28] T.SEBASTIAN M. ABO₃ TYPE PEROVSKITES. *Dielectric Materials for Wireless Communication*. Amsterdam: Elsevier; 2008. p. 161-203.

[29] Peña MA, Fierro JLG. Chemical Structures and Performance of Perovskite Oxides. *Chemical Reviews*. 2001;101(7):1981–2018.

[30] Zaccaria V. SOFC degradation model for cyber-physical simulation and control of fuel cell gas turbine hybrid systems: Malardalen University; 2017.

[31] Tatsumi I, Hideaki MY, Takita. Effects of rare earth cations doped for La site on the oxide ionic conductivity of LaGaO₃-based perovskite type oxide *Solid State Ionics*. 1995;79:147-51.

[32] Pelosato R, Cristiani C, Dotelli G, Latorrata S, Ruffo R, Zampori L. Co-precipitation in aqueous medium of La_{0.8}Sr_{0.2}Ga_{0.8}Mg_{0.2}O_{3-δ} via inorganic precursors. *Journal of Power Sources*. 2010;195(24):8116-23.

[33] Choi HJ, Kim M, Neoh KC, Jang DY, Kim HJ, Shin JM, Kim G-T, Shim JH. High-Performance Silver Cathode Surface Treated with Scandia-Stabilized Zirconia Nanoparticles for Intermediate Temperature Solid Oxide Fuel Cells. *Advanced Energy Materials*. 2017;7(4).

[34] Tao S, Irvine JTS. Catalytic properties of the perovskite oxide La_{0.75}Sr

$_{0.25}\text{Cr}_{0.5}\text{Fe}_{0.5}\text{O}_{3-\delta}$ in relation to its potential as a solid oxide fuel cell anode material. Chemistry of Materials. 2004;16(21):4116 - 21.

[35] Aliotta C, Liotta LF, Deganello F, La Parola V, Martorana A. Direct methane oxidation on $\text{La}_{1-x}\text{Sr}_x\text{Cr}_{1-y}\text{Fe}_y\text{O}_{3-\delta}$ perovskite-type oxides as potential anode for intermediate temperature solid oxide fuel cells. Applied Catalysis B: Environmental. 2016;180:424-33.

[36] Ruiz-Morales JC, Marrero-López D, Gálvez-Sánchez M, Canales-Vázquez J, Savaniu C, Savin SN. Engineering of materials for solid oxide fuel cells and other energy and environmental applications. Energy & Environmental Science. 2010;3(11).

[37] Bilal Hanif M, Motola M, qayyum S, Rauf S, khalid A, Li C-J, Li C-X. Recent advancements, doping strategies and the future perspective of perovskite-based solid oxide fuel cells for energy conversion. Chemical Engineering Journal. 2022;428.

[38] Vincent AL, Luo J-L, Chuang KT, Sanger AR. Promotion of activation of CH_4 by H_2S in oxidation of sour gas over sulfur tolerant SOFC anode catalysts. Applied Catalysis B: Environmental. 2011.

[39] Vincent A, Luo J-L, Chuang KT, Sanger AR. Effect of Ba doping on performance of LST as anode in solid oxide fuel cells. Journal of Power Sources. 2010;195(3):769-74.

[40] Zhao H, Gao F, Li X, Zhang C, Zhao Y. Electrical properties of yttrium doped strontium titanate with A-site deficiency as potential anode materials for solid oxide fuel cells. Solid State Ionics. 2009;180(2-3):193-7.

[41] Du Z, Zhao H, Zhou X, Xie Z, Zhang C. Electrical conductivity and cell performance of $\text{La}_{0.3}\text{Sr}_{0.7}\text{Ti}_{1-x}\text{Cr}_x\text{O}_{3-\delta}$ perovskite oxides used as anode and interconnect material for SOFCs. International Journal of Hydrogen Energy. 2013;38(2):1068-73.

[42] Rath MK, Ahn B-G, Choi B-H, Ji M-J, Lee K-T. Effects of manganese substitution at the B-site of lanthanum-rich strontium titanate anodes on fuel cell performance and catalytic activity. Ceramics International. 2013;39(6):6343-53.

[43] Shiqiang HA, Petric. Evaluation of yttrium-doped SrTiO_3 as an anode for solid oxide fuel cells. Journal of the European Ceramic Society. 2002;22(9-10):1673-81.

[44] Cui S-H, Li J-H, Zhou X-W, Wang G-Y, Luo J-L, Chuang KT, Bai Y, Qiao L-J. Cobalt doped $\text{LaSrTiO}_{3-\delta}$ as an anode catalyst: effect of Co nanoparticle precipitation on

SOFCS operating on H₂S-containing hydrogen. *Journal of Materials Chemistry A*. 2013;1(34).

[45] Atta NF, Galal A, El-Ads EH. *Perovskite Nanomaterials – Synthesis, Characterization, and Applications*. InTech; 2016.

[46] Assirey EAR. Perovskite synthesis, properties and their related biochemical and industrial application. *Saudi Pharm J*. 2019;27(6):817-29.

[47] Li Q, Zheng Y, Sun Y, Li T, Xu C, Wang W, Chan SH. Understanding the occurrence of the individual CO₂ electrolysis during H₂O-CO₂ co-electrolysis in classic planar Ni-YSZ/YSZ/LSM-YSZ solid oxide cells. *Electrochimica Acta*. 2019;318:440-8.

[48] Zhang W, Zheng Y, Yu B, Wang J, Chen J. Electrochemical characterization and mechanism analysis of high temperature Co-electrolysis of CO₂ and H₂O in a solid oxide electrolysis cell. *International Journal of Hydrogen Energy*. 2017;42(50):29911-20.

[49] Wang Y, Liu T, Fang S, Chen F. Syngas production on a symmetrical solid oxide H₂O/CO₂ co-electrolysis cell with Sr₂Fe_{1.5}Mo_{0.5}O₆-Sm_{0.2}Ce_{0.8}O_{1.9} electrodes. *Journal of Power Sources*. 2016;305:240-8.

[50] Dogu D, Meyer KE, Fuller A, Gunduz S, Deka DJ, Kramer N, Co AC, Ozkan US. Effect of lanthanum and chlorine doping on strontium titanates for the electrocatalytically-assisted oxidative dehydrogenation of ethane. *Applied Catalysis B: Environmental*. 2018;227:90-101.

[51] Shannon RD. Revised effective ionic radii and systematic studies of interatomic distances in halides and chalcogenides. *Acta Crystallographica Section A*. 1976;32(5):751-67.

[52] Napolitano F, Lamas DG, Soldati A, Serquis A. Synthesis and structural characterization of Co-doped lanthanum strontium titanates. *International Journal of Hydrogen Energy*. 2012;37(23):18302-9.

[53] Saeed A, Ruthramurthy B, Yong WH, Hoong OB, Ban TK, Kwang YH. Structural and dielectric properties of iron doped barium strontium titanate for storage applications. *Journal of Materials Science: Materials in Electronics*. 2015;26(12):9859-64.

[54] Shah MAKY, Rauf S, Zhu B, Mushtaq N, Yousaf M, Lund PD, Xia C, Asghar MI. Semiconductor Nb-Doped SrTiO_{3-δ} Perovskite Electrolyte for a Ceramic Fuel Cell. *ACS*

Applied Energy Materials. 2021;4(1):365-75.

[55] Huan Y, Li Y, Yin B, Ding D, Wei T. High conductive and long-term phase stable anode materials for SOFCs: A_2FeMoO_6 ($A = Ca, Sr, Ba$). Journal of Power Sources. 2017;359:384-90.

[56] Li X, Zhao H, Gao F, Zhu Z, Chen N, Shen W. Synthesis and electrical properties of Co-doped $Y_{0.08}Sr_{0.92}TiO_{3-\delta}$ as a potential SOFC anode. Solid State Ionics. 2008;179(27-32):1588-92.

[57] YANG W-D. X-ray photoelectron spectroscopy and electrical properties studies of La_2O_3 -doped strontium titanate ceramics prepared by sol-precipitation method. Journal of Materials Science. 1999;34:3533-44.

[58] Padilla-Campos L, Diaz-Droguett DE, Lavín R, Fuentes S. Synthesis and structural analysis of Co-doped $BaTiO_3$. Journal of Molecular Structure. 2015;1099:502-9.

[59] Gao R, Yu G, Chen W, Li GD, Gao S, Zhang Z, Shen X, Huang X, Zou X. Host-Guest Interaction Creates Hydrogen-Evolution Electrocatalytic Active Sites in 3d Transition Metal-Intercalated Titanates. ACS Appl Mater Interfaces. 2018;10(1):696-703.

[60] Jia A, Su Z, Lou L-L, Liu S. Synthesis and characterization of highly-active nickel and lanthanum co-doped $SrTiO_3$. Solid State Sciences. 2010;12(7):1140-5.

[61] Wang H, Zhang X, Zhang W, Wei Z, Guan K, Meng J, Meng F, Meng J, Liu X. Enhancing catalysis activity of $La_{0.6}Sr_{0.4}Co_{0.8}Fe_{0.2}O_{3-\delta}$ cathode for solid oxide fuel cell by a facile and efficient impregnation process. International Journal of Hydrogen Energy. 2019;44(26):13757-67.

[62] Yao C, Meng J, Liu X, Zhang X, Meng F, Wu X, Meng J. Effects of Bi doping on the microstructure, electrical and electrochemical properties of $La_{2-x}Bi_xCu_{0.5}Mn_{1.5}O_6$ ($x = 0, 0.1$ and 0.2) perovskites as novel cathodes for solid oxide fuel cells. Electrochimica Acta. 2017;229:429-37.

[63] Zhang L, Hu S, Zhu X, Yang W. Electrochemical reduction of CO_2 in solid oxide electrolysis cells. Journal of Energy Chemistry. 2017;26(4):593-601.

[64] Zhu C, Liu J, Yu X, Zhang Y, Zhang Y, Jiang X, Wang S, Wang Q, Dong P. Enhance the electrochemical performance of $Li_4Ti_5O_{12}$ with Co doping via a facile mechanical activation strategy. Journal of Materials Science: Materials in Electronics.

2019;30(6):5866-73.

- [65] Li J, Lv T, Hou N, Li P, Yao X, Fan L, Gan T, Zhao Y, Li Y. Molybdenum substitution at the B-site of lanthanum strontium titanate anodes for solid oxide fuel cells. *International Journal of Hydrogen Energy*. 2017;42(34):22294-301.
- [66] Du Z, Zhao H, Shen Y, Wang L, Fang M, Świerczek K, Zheng K. Evaluation of $\text{La}_{0.3}\text{Sr}_{0.7}\text{Ti}_{1-x}\text{Co}_x\text{O}_3$ as a potential cathode material for solid oxide fuel cells. *J Mater Chem A*. 2014;2(26):10290-9.
- [67] Shan K, Guo X-M. Electrical conduction behavior of A-site deficient (Y, Fe) co-doped SrTiO_3 mixed ionic–electronic conductor. *Materials Letters*. 2013;113:126-9.
- [68] Abdi M, Mahdikhah V, Sheibani S. Visible light photocatalytic performance of La-Fe co-doped SrTiO_3 perovskite powder. *Optical Materials*. 2020;102.
- [69] Kajimoto R, Nakamura M, Murai N, Shamoto SI, Honda T, Ikeda K, Otomo T, Hata H, Eto T, Noda M, Kuwahara H, Okuda T. Elastic and dynamical structural properties of La and Mn-doped SrTiO_3 studied by neutron scattering and their relation with thermal conductivities. *Sci Rep*. 2018;8(1):9651.
- [70] Introduction to Electrochemical Impedance Spectroscopy (EIS) [Internet]. [cited 14 Dec 2022]. Available from: https://www.admiralinstruments.com/_files/ugd/dc5bf5_28e4de359f3540ffa1980971fb63be93.pdf.
- [71] Kim Y-M, Kim-Lohsoontorn P, Baek S-W, Bae J. Electrochemical performance of unsintered $\text{Ba}_{0.5}\text{Sr}_{0.5}\text{Co}_{0.8}\text{Fe}_{0.2}\text{O}_{3-d}$, $\text{La}_{0.6}\text{Sr}_{0.4}\text{Co}_{0.8}\text{Fe}_{0.2}\text{O}_{3-d}$, and $\text{La}_{0.8}\text{Sr}_{0.2}\text{MnO}_{3-d}$ cathodes for metal-supported solid oxide fuel cells. *International Journal of Hydrogen Energy*. 2011;36(4):3138-46.
- [72] Yan Y, Fang Q, Blum L, Lehnert W. Performance and degradation of an SOEC stack with different cell components. *Electrochimica Acta*. 2017;258:1254-61.
- [73] Li X, Zhao H, Xu N, Zhou X, Zhang C, Chen N. Electrical conduction behavior of La, Co co-doped SrTiO_3 perovskite as anode material for solid oxide fuel cells. *International Journal of Hydrogen Energy*. 2009;34(15):6407-14.
- [74] El Roubi WMA. Selective adsorption and degradation of organic pollutants over Au decorated Co doped titanate nanotubes under simulated solar light irradiation.

Journal of the Taiwan Institute of Chemical Engineers. 2018;88:201-14.

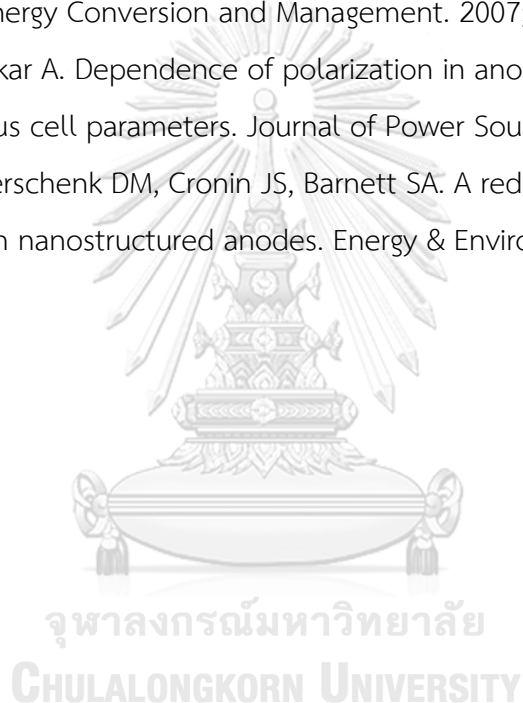
[75] Mousavi Ghahfarokhi SE, Ranjbar F, Zargar Shoushtari M. A study of the properties of $\text{SrFe}_{12-x}\text{Co}_x\text{O}_{19}$ nanoparticles. Journal of Magnetism and Magnetic Materials. 2014;349:80-7.

[76] Hui R, Berghaus JO, Decès-Petit C, Qu W, Yick S, Legoux J-G, Moreau C. High performance metal-supported solid oxide fuel cells fabricated by thermal spray. Journal of Power Sources. 2009;191(2):371-6.

[77] Zhang X, Li G, Li J, Feng Z. Numerical study on electric characteristics of solid oxide fuel cells. Energy Conversion and Management. 2007;48(3):977-89.

[78] Zhao F, Virkar A. Dependence of polarization in anode-supported solid oxide fuel cells on various cell parameters. Journal of Power Sources. 2005;141(1):79-95.

[79] Zhan Z, Bierschenk DM, Cronin JS, Barnett SA. A reduced temperature solid oxide fuel cell with nanostructured anodes. Energy & Environmental Science. 2011;4(10).



APPENDIX

APPENDIX A: Crystallite size

The crystallite size of synthesized powder was calculated using the Scherrer equation as shown in Fig. A.1 and Eq. (A.1), respectively.

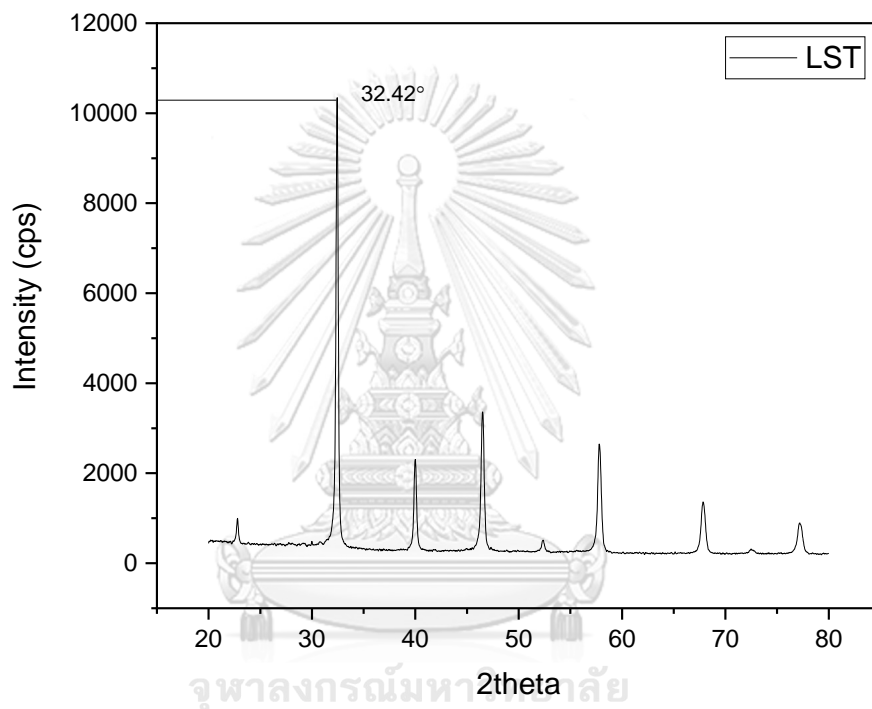


Figure A.1 XRD pattern of LST

$$D = \frac{K\lambda}{\beta_{FWHM} \cos \theta} \quad (A.1)$$

Where K is Scherrer constant (a typical value of 0.94); λ is the wavelength of x-ray (in this case: 0.1541nm for Cu K-alpha); β_{FWHM} is the full width at half-maximum of the diffraction peak, θ is the Bragg angle and D is crystallite size(nm).

θ calculation:

$$2\theta = 32.42 \text{ and } \theta = 16.21$$

β calculation: β value can be calculated from FWHM that interpolate from XRD results. The FWHM from XRD at 32.42° is 0.2729.

$$\beta = (\text{FWHM} \times 2\pi)/360$$

$$\beta = (0.2729 \times 2\pi)/360 = 0.00476$$

Crystallite size of LST at $2\theta = 32.42^\circ$:

$$D = (0.94 \times 0.1541) / (0.00476 \times \cos(16.21)) = 31.69$$

APPENDIX B: Lattice parameter

The lattice parameter was calculated using the Bragg's law equation as shown in Eq. (B.1) and Eq. (B.2), respectively.

$$n\lambda = 2d\sin\theta \quad (\text{B.1})$$

where n is an integer; λ is the wavelength of the x-ray (1.54 \AA); d is the spacing of the crystal layers; and θ is the angle between incident ray and the scatter plane Lattice parameter equation for cubic structure:

$$\left(\frac{1}{d^2}\right) = (h^2 + k^2 + l^2) \left(\frac{1}{a^2}\right) \quad (\text{B.2})$$

when d is the spacing of the crystal layers; a is lattice parameter; and h, k, l are spacing between lattice planes θ and plane (h, k , and l) were found from XRD pattern and data of JCPDS respectively. For LST, θ and plane (h, k , and l) were used to calculating the lattice parameter as below.

d calculation:

$$n\lambda = 2d\sin\theta$$

$$\left(\frac{1}{d^2}\right) = 4\sin^2\theta / \lambda^2$$

At $2\theta = 32.42$ and $\theta = 16.21$

$$\left(\frac{1}{d^2}\right) = 4\sin^2(16.21) / 1.54^2 = 0.1314$$

Then substituted $\left(\frac{1}{d^2}\right)$ and (h, k, l) into Eq. (B.2)

$$\text{At } (1, 1, 0) \quad 0.1314 = (1^2 + 1^2 + 0^2) \left(\frac{1}{a^2}\right)$$

Hence, lattice parameter: $a = 3.901 \text{ \AA}$

APPENDIX C: Tolerance factor

The Goldschmidt tolerance factor (t) was calculated using Eq. (C.1):

$$t = \frac{r_A + r_B}{\sqrt{2}(r_B + r_O)} \quad (C.1)$$

where r_A , r_B , and r_O are the ionic radii of the A-site cation, B-site cation and oxygen ion, respectively.

Table C.1 Ionic charge, coordination number and ionic radius of concerned metals

Metal	Ionic charge	Coordination number	Ionic radius (Å)
La	3+	12	1.36
Sr	2+	12	1.44
Ti	4+	6	0.605
Co	2+	6	0.745
O	2-	6	1.4

As Eq. (C.1) the tolerance factor of perovskite anode such as $\text{LSTC}_{0.10}$ was calculated as below.

$$t = \frac{(1.36 \times 0.3) + (1.44 \times 0.7) + 1.4}{\sqrt{2} [(0.605 \times 0.90) + (0.745 \times 0.10) + 1.4]} = 0.9862$$

VITA

NAME	Natthamon Nuengjumnong
DATE OF BIRTH	24 October 1997
PLACE OF BIRTH	Chonburi
INSTITUTIONS ATTENDED	Faculty of Engineering, Chulalongkorn University Faculty of Engineering, Mahidol University
HOME ADDRESS	84 , Banbueng, Banbueng, Chonburi 20170

